Sugar phosphate-mediated inhibition of peptidoglycan precursor synthesis

Megan R. Keller[1,3]*, Vijay Soni[4], Megan Brown[4], Kelly M. Rosch[1,3], Anas Saleh[4], Kyu Rhee[3,4]*, and Tobias Doerr[1,2,3]*

[1] Weill Institute for Cell and Molecular Biology, Cornell University, Ithaca, NY 14853, USA

[2] Department of Microbiology, Cornell University, Ithaca NY 14853, USA

[3] Cornell Institute of Host-Microbe Interactions and Disease, Cornell University, Ithaca NY 14853, USA

[4] Department of Medicine, Division of Infectious Diseases, Weill Cornell Medicine, New York, NY 10021

* corresponding authors: mrk269@cornell.edu, kyr9001@med.cornell.edu and tdoerr@cornell.edu

Keywords: Gram-negative bacteria, bacterial metabolism, antibiotic resistance, stress, enzyme inhibitor

Abstract

Antibiotic tolerance, the widespread ability of diverse pathogenic bacteria to sustain viability in the presence of typically bactericidal antibiotics for extended time periods, is an understudied steppingstone towards antibiotic resistance. The Gram-negative pathogen *Vibrio cholerae*, the causative agent of cholera, is highly tolerant to β-lactam antibiotics. We previously found that the disruption of glycolysis, via deletion of *pgi* (*vc0374*, glucose-6-phosphate isomerase), resulted in significant cell wall damage and increased sensitivity towards β-lactam antibiotics. Here, we uncover the mechanism of this resulting damage. We find that glucose causes growth inhibition, partial lysis, and a damaged cell envelope in Δ*pgi*. Supplementation with N-acetylglucosamine, but not other carbon sources (either from upper glycolysis, TCA cycle intermediates, or cell wall

precursors) restored growth, re-established antibiotic resistance towards β-lactams, and recovered cellular morphology of a *pgi* mutant exposed to glucose. Targeted metabolomics revealed the cell wall precursor synthetase enzyme GlmU (*vc2762*, coding for the bifunctional enzyme that converts glucosamine-1P to UDP-GlcNAc) as a critical bottleneck and mediator of glucose toxicity in Δ*pgi*. *In vitro* assays of GlmU revealed that sugar phosphates (primarily glucose-1-phosphate) inhibit the acetyltransferase activity of GlmU (likely competitively), resulting in compromised PG and LPS biosynthesis. These findings identify GlmU as a critical branchpoint enzyme between central metabolism and cell envelope integrity and reveal the molecular mechanism of Δ*pgi* glucose toxicity in *Vibrio cholerae*.

Importance

Sugar-phosphate toxicity is a well characterized phenomenon that is seen within diverse bacterial species, and yet the molecular underpinnings remain elusive. We previously discovered that disrupting *Vibrio cholerae's* ability to eat glucose (by disrupting the *pgi* gene), also resulted in a damaged cell envelope. Upon deletion of *pgi*, glucose-phosphate levels rapidly build and inhibit the enzymatic activity of GlmU, a key step of bacterial peptidoglycan precursor synthesis. GlmU inhibition causes enhanced killing by antibiotics and a pronounced cell envelope defect. Thus, GlmU serves as a prime target for novel drug development. This research opens new routes through which central metabolism and sugar-phosphate toxicity modulate antibiotic susceptibility.

Introduction

48 The antibiotic susceptibility spectrum, including resistance, tolerance, and persistence,
49 continues to be a massive clinical threat (1, 2). Ranging from outright resistance, i.e.
50 growth in the presence of antibiotics, to bacterial languishing (surviving and tolerating
51 exposure antibiotics for a prolonged time), to having only a subset of the bacterial
52 population persist and able to survive antibiotic exposure, there are many ways in which
53 bacteria can respond to antibiotics (3–5). Furthermore, there has been an increase in
54 studies finding that tolerance and persistence are steppingstones towards full resistance
55 (6, 7). Discovering and understanding these midway points is needed to find novel
56 potential antibiotic development routes, in order to solve this pressing issue facing our
57 health care system.
58
59 With many common antibiotic development routes already being explored with varying
60 degrees of success, interest in processes long overlooked (like tolerance) has recently
61 surged. Particularly the contribution of central metabolic pathways to antibiotic
62 susceptibility and infection outcomes have received considerable attention (8–13).
63 Central carbon metabolism, for example, consists of interconnected pathways that
64 ultimately produce energy for life as well as crucial precursors for biosynthesis of key
65 macromolecules; most of these pathways are almost universally conserved (14–16).
66 Glycolysis (more specifically, the Embden-Meyerhof-Parnas (EMP) pathway), the TCA
67 cycle, and the pentose phosphate pathway are all vital carbon utilization networks found
68 in virtually all extant species (17). Their interaction with many other cellular pathways
69 (including cell envelope homeostasis) makes central carbon metabolism a potential

central hub for determining antibiotic susceptibility, and consequently for developing novel forms of therapeutic intervention.

In a previous study, we discovered that deletion of *pgi*, a key enzyme in central carbon metabolism (EMP pathway) involved in the bidirectional conversion of glucose-6P to fructose-6P, causes cell wall damage and an increase in susceptibility to cell wall-acting antibiotics in the hypertolerant Gram-negative pathogen *Vibrio cholerae* (10). We found that these defects were associated with the intracellular accumulation of sugar phosphates and could be relieved by addition of the external cell wall precursor, N-acetylglucosamine (GlcNAc). Here, we sought to determine the molecular mechanism underlying sugar toxicity in the Δ*pgi* mutant. Genetic, metabolomic, and biochemical evidence suggest that glucose-1-phosphate inhibits GlmU function, thereby compromising the formation of UDP-GlcNAc, which results in inhibition of both peptidoglycan and potentially LPS biosynthesis. Our data thus identifies a new potential antibiotic target in *V. cholerae*, supporting the idea that metabolic disruptions could be weaponized to combat antibiotic tolerance and resistance.

Results

Glucose toxicity in a Δ*pgi* mutant manifests as morphological and functional damage to the cell envelope. To understand the negative effects caused by the addition of glucose in a Δ*pgi* mutant, we measured cellular morphology as well as survival in response to increasing glucose concentrations. WT, Δ*pgi*, and its complemented derivative were grown to exponential phase in M9 (minimal medium) supplemented with

0.2% casamino acids, followed by addition of increasing concentrations of glucose (0%, 0.02%, 0.2%, and 2%). Phase contrast microscopy after 3 hours of growth at 37°C revealed a notable morphology defect in Δ*pgi* (**Fig. 1A**), in essence recapitulating our previous observations in a more defined medium (10). An increase in glucose concentrations correlated with enhanced apparent cell death (visible as cell debris) and morphological defects, a typical response to inhibition of cell wall synthesis (18–21). To visualize cellular lysis further, we plated stationary phase cells on an LB agar plate with 0.2% glucose and 20 µg/mL of the cell impermeable β-galactosidase (LacZ) substrate CPRG (chlorophenol red-β-D-galactopyranoside) and incubated the plate overnight. Lysed cells will leak cytoplasmic LacZ into the medium and CPRG is hydrolyzed, resulting in a deep-red color change (22). While the Δ*pgi* mutant was able to form colonies on this plate, it demonstrated markedly enhanced cell lysis in the presence of glucose (**Fig. S1**). The combination of morphological defects and lysis suggests that both lipopolysaccharide (LPS) and peptidoglycan (PG) synthesis are at least partially affected in glucose-treated *pgi* mutants, as ordinarily PG synthesis inhibition results in spheroplast formation and little lysis in *V. cholerae*.

We next sought to assess the viability of Δ*pgi* cells in increasing glucose concentrations to determine the extent of glucose toxicity. Following the same experimental setup as described previously, increasing glucose concentrations were added to medium containing M9 + 0.2% casamino acids. Cells were incubated for 3 hours with defined glucose addition and then were serially diluted and plated on M9 agar containing 0.2% casamino acids. After an overnight incubation at 37°C, CFU/mL were counted. We noticed

a slight but significant decrease in cell viability in a Δ*pgi* mutant that worsened with increasing glucose concentrations, reaching 10-fold at 2% glucose, while the WT remain unaffected (**Fig. 1B**). Collectively, these data indicate that glucose toxicity in a Δ*pgi* mutant results in a damaged cellular envelope.

External N-Acetylglucosamine is sole carbon source to complement Δ*pgi* in glucose. We previously found that exogenous N-acetylglucosamine (GlcNAc) rescues Δ*pgi* defects in LB (10). However, since these experiments were done in LB (which produces a messy, poorly characterized physiology (23)), we sought to utilize a more chemically defined growth medium. In principle, the observed growth defect of Δ*pgi* in glucose could be due to either a decrease in cell wall precursor synthesis (which branches from glycolysis at fructose-6-phosphate, the product Pgi generates), or reduced flux into lower glycolysis, causing energy imbalance. Indeed, glucose phosphate toxicity (albeit in response to the glucose phosphate analog alpha-MG) in *E. coli* can be overcome by adding glycolytic intermediates, including fructose-6-phosphate (24). To test these ideas, we supplemented Δ*pgi* grown on M9 + 0.2% glucose with a panel of carbon sources, covering the spectrum of glycolysis and cell wall synthesis (**Fig. 2A**). After confirming cells could import and utilize these different carbon sources using a growth assay (**Fig. S2A**), we then plated serial dilutions of overnight cultures grown in M9 + 0.2% casamino acids, on M9 agar plates with glucose and the described carbon sources to assess rescue effects on the *pgi* mutant.

Interestingly, only GlcNAc could rescue Δ*pgi* growth and morphology in the presence of glucose (**Fig. 2A-B**). Neither fructose (which, upon import, gets converted to fructose-6-phosphate), pyruvate, nor succinate or glycerol rescued the Δ*pgi* growth defect on glucose, suggesting that Δ*pgi* glucose susceptibility is not primarily due to energy imbalance caused by disruption of glycolysis. We previously reported that a Δ*pgi* mutant was more sensitive to cell-wall targeting antibiotics (10). Therefore, we also sought to investigate the effect of GlcNAc on antibiotic susceptibility. Here, we added 0.2% GlcNAc to LB agar plates and measured the zone of inhibition in response to two β-lactam antibiotics (penicillin G and carbenicillin) (**Fig. 2C**). Addition of GlcNAc increased resistance to the Δ*pgi* mutant (though not to the WT). Thus, GlcNAc supplementation restores all characterized defects of a Δ*pgi* mutant.

Interestingly, MurNAc, another cell wall fragment, did not restore growth (**Fig. 2A**). This was curious, as both MurNAc and GlcNAc are cell wall precursors. MurNAc import occurs more upstream of *pgi* activity than GlcNAc and requires more steps to convert it into the common cell wall precursor glucosamine-6P. It is possible that the enzyme responsible for converting MurNAc-6P to GlcNAc-6P, MurQ, or the MurNAc transporter, MurP, are too inefficient for restoring optimal carbon flux, or not expressed under our growth conditions. Consistent with an inefficiency of MurNAc utilization, growth on MurNAc as sole carbon source resulted in much poorer yield than growth on GlcNAc (**Fig. S2**).

Genetic manipulation of biosynthesis pathways reveals PG precursor demand in Δ*pgi*. We then began to genetically explore the GlcNAc import pathway and its

connections between *pgi* and cell wall synthesis (summarized in **Fig. 3A**). We previously reported that glucose-6-phosphate accumulates in a *pgi* mutant; however, our untargeted metabolomics approach could not distinguish between glucose-6-phosphate (G6P) and glucose-1-phosphate (G1P). To dissect these two sugar phosphate species further, we constructed gene deletion and overexpression strains of the enzyme that converts G6P into G1P, *pgcA*, (*vc2095*), also known as *pgm* in *E. coli,* in a Δ*pgi* background. We hypothesized that reducing or boosting glucose-phosphate levels might mitigate or exacerbate *pgi* mutant phenotypes. We were additionally interested in the branch point enzymes NagB (*vca1025*) and GlmS (*vc0487*) for their role in regulating flux between glycolysis and cell-wall synthesis. We reasoned that by siphoning away early PG precursor metabolites (i.e. Glucosamine-6P) into glycolysis (via NagB), a *pgi* mutant would experience more defects, while GlmS overexpression should have the opposite effect. We thus tested these strains for their ability to modulate Δ*pgi* phenotypes. First, we tested PenG antibiotic susceptibility by measuring the zone of inhibition (**Fig. 3B**). *glmS* overexpression significantly reduced Δ*pgi* PenG sensitivity, suggesting that directing metabolic flux towards PG precursors and away from glycolysis was beneficial. Conversely, overexpression of *nagB* and *pgcA* tendentially enhanced PenG sensitivity, though this was not statistically significant (**Fig. 3A**).

Next, we turned to another phenotype, i.e. Δ*pgi*'s reduced survival in the presence of glucose. We thus treated the strains with either 0.2% or 2% glucose for 3 hours and then plated on M9 + 0.2% casamino acids (**Fig. 3C**). In both glucose concentrations, overexpressing *nagB* in a Δ*pgi* background resulted in significantly lower cell viability. At

higher glucose levels, overexpression of *pgcA* in Δ*pgi* also became statistically significant in reducing cell viability. Collectively, these data point to a contribution of G1P in sugar phosphate toxicity of Δ*pgi and* suggest that carbon flux away from glycolysis helps this mutant, while flux away from cell wall precursor synthesis exacerbates its growth defect.

Targeted metabolomics suggest a metabolite bottleneck around GlmU in glucose-treated *pgi* mutant cells. To further characterize the metabolic disruptions observed in a Δ*pgi* mutant and how the addition of GlcNAc could shift these metabolites, we conducted targeted metabolomics upon glucose exposure in M9 medium + CAA. Three hours after addition of either 0.2% glucose or a combination of 0.2% glucose and 0.2% GlcNAc, cells were pelleted, and metabolites were extracted using methanol. Samples were analyzed using LC-MS (see Methods and Materials), and peaks were compared to pure chemical standards. Upon normalizing the data to the casamino acid conditions, we noted a sharp increase in glucose-1P and glucose-6P, consistent with the *pgi* mutant's inability to metabolize glucose through the EMP glycolysis pathway. The WT, but not Δ*pgi*, experienced an increase in pyruvate levels upon glucose addition. The combination of increased pyruvate and reduced G6P/G1P levels (and indeed very low F6P levels) in the WT perhaps indicates highly efficient upper glycolysis, which encounters a bottleneck at pyruvate processing. The relative lack of increase in pyruvate upon glucose addition in Δ*pgi* suggests that non-EMP pathways for glucose utilization (e.g., pentose phosphate pathway), and/or gluconeogenesis, may be inefficient in *V. cholerae,* at least under the conditions tested here. We also observed a sharp rise in glucosamine-1P levels (16-fold change), and a sharp, 36-fold decrease in UDP-GlcNAc, when Δ*pgi* was grown in medium

containing glucose, compared to WT (**Fig. 4A**). Thus, the described sugar toxicity likely results from the inhibition of the enzyme converting glucosamine-1P to UDP-GlcNAc, which is GlmU (**Fig. 4B**). This bottleneck was slightly improved upon the addition of GlcNAc to the growth medium, suggesting GlcNAc-mediated relief of this inhibition. As expected from the pathway metabolizing external GlcNAc (**Fig. 3B**), the addition correlated with a slight increase in glucosamine-6P (into which external GlcNAc is converted by *V. cholerae* through the action of the NagE transporter and NagA deacetylase) (25).

Plausibly, the accumulation of glucose-1P and/or glucose-6P in the Δ*pgi* mutant competitively inhibits GlmU, downregulating cell wall synthesis. There is evidence of a similar effect in *Mycobacterium tuberculosis*, where at least glucose-1P competitively inhibits GlmU *in vitro* (26). Glucose-1P levels did not change (**Fig. 4A**) upon addition of GlcNAc, which may indicate that GlcNAc addition does not stop sugar phosphate accumulation, but rather circumvents PG precursor synthesis inhibition by supplying more substrate (which would suggest competitive inhibition). Fructose-6P levels in both WT and Δ*pgi* cells were significantly lower in glucose-containing medium. It is possible that flux into the TCA cycle and downstream respiration is faster in the presence of glucose, which causes a net relative decrease in F6P levels relative to growth in casamino acids (gluconeogenic conditions).

If GlmU is competitively inhibited by glucose phosphates, it should be possible to circumvent this inhibition by increasing the abundance of GlmU. Therefore, we next

sought to genetically explore the role of GlmU by creating an overexpression construct in a Δ*pgi* background. Overexpression of *glmU* from a high copy number plasmid (see Methods and Materials), caused a significant increase in cell viability in the presence of glucose in comparison to Δ*pgi* alone (**Fig. 4C**). While there still was a decrease in overall survival, even when expressing *glmU* excessively, this can be explained by the glucose phosphate inhibition logic. We previously measured an over 200x increase in G1P/G6P in Δ*pgi* when grown in LB (10); adding a few more GlmU molecules is likely not sufficient to compensate for the intracellular flooding of G1P/G6P, especially when grown in medium with high glucose concentrations. We also overexpressed *glmU* from an overnight culture and plated serial dilutions on M9 + 0.2% CAA supplemented with either 0.02% glucose or 0.2% glucose (**Fig. 4D**). GlmU overexpression significantly improved Δ*pgi* plating efficiency on glucose, particularly at the lower glucose concentration, again supporting the idea of GlmU being the target of glucose toxicity in the Δ*pgi* mutant.

***In vitro* biochemical validation of GlmU inhibition by glucose-1P.** We next conducted an *in vitro* biochemistry assay using purified *V. cholerae* GlmU, to test whether G1P/G6P inhibition was direct. To this end, we tested a panel of G1P and G6P concentrations designed to mimic the glucose concentrations previously measured in Δ*pgi* (10) in a biochemical assay containing purified GlmU, as well as the reactants Acetyl-CoA, glucosamine-1-phosphate and UTP. After 30 min at 30°C, the reaction was stopped and analyzed for the emergence of the product of the GlmU reaction, UDP-GlcNAc, using LC-MS. Upon addition of increasing concentrations of G1P, but not G6P (**Fig. S3A**) to the reaction mix, we observed a significant decrease in UDP-GlcNAc abundance starting at

31.25mM of G1P, and near complete inhibition at 250mM (**Fig. 5C**). We also measured the intermediate product of GlmU's bifunctional reaction, GlcNAc-1P. We found that at higher concentrations of G1P, GlcNAc-1P was also significantly reduced, suggesting that it is the acetyl-transferase activity of GlmU that is primarily affected by G1P inhibition.

Molecular modeling reveals putative target site for glucose phosphate inhibition. We next sought to model the observed inhibition of glucose-1P against GlmU. While Alphafold3 is a powerful and accessible tool for modeling protein-ligand interactions, it is not well suited for our study as it is unable to model glucose-1P (27). Instead, we turned to Chai Discovery, a new online modeling program that predicts both protein multimers and protein-ligand binding (28). We obtained multiple models of predicted binding sites for both GlmU's natural substrate, glucosamine-1P, but also its presumed inhibitor, glucose-1P, within the trimeric form of GlmU. Visualization of these molecular models revealed that glucosamine-1-P engages in polar interactions with Arg330, Lys348, Tyr363, Asn374, Asn383, and Lys389 (**Fig. 6A**). This model returned pTM and ipTM scores of 0.9556 and 0.9388, respectively; pTM scores > 0.5 and ipTM scores > 0.8 are considered confident predictions (29). Sequence alignments with $GlmU^{EC}$ and $GlmU^{Mtb}$, which have well characterized active sites (26, 30), indicate that the modeled residues likely form the acetyltransferase active site in $GlmU^{VC}$ (**Fig. S5A-C**). Additionally, structural alignments of $GlmU^{VC}$ to $GlmU^{EC}$ and $GlmU^{Mtb}$ indicate that the structure of GlmU is highly conserved across diverse organisms. Molecular modeling of the putative interaction between GlmU and glucose-1-P revealed a binding site at the same location as the natural substrate, indicating that glucose-1-P may competitively inhibit GlmU (**Fig.**

6A). This model returned similarly high pTM and ipTM scores (0.9549 and 0.9376 respectively). While there were some predictions that modeled G1P within the uridyltransferase pocket, the strength of the polar interactions were not as robust as the models that predicted G1P to bind within the acetyltransferase pocket (**Fig. S4B**). We additionally examined the predicted binding with glucose-6P, and found while it does bind in a similar fashion as glucose-1P, the pTM and ipTM scores were lower (**Fig.S4C-D**). How the phosphate location on the glucose molecule elicits such a drastically different inhibition response and binding affinity, remains to be explored. Together, this strongly suggests that G1P accumulation competitively inhibits the acetyltransferase activity of GlmU.

Discussion

Sugar-phosphate stress and its associated cellular defects remain underexplored in the context of antibiotic susceptibility. Here, we present data that elucidate the mechanism of glucose poisoning in *Vibrio cholerae*. We previously found that *pgi* mutation results in pronounced cell wall damage and concomitant increase in susceptibility to β-lactam antibiotics (10). In this study, we show that glucose toxicity in Δ*pgi* is due to (likely competitive) inhibition of GlmU (a key step in PG precursor synthesis) by sugar phosphate species. Sugar-phosphate toxicity has been studied for the past 7 decades (31–36), yet the mechanisms for glucose-related toxicity appear to be diverse, species-dependent, and poorly-understood (37, 38). In *B. subtilis,* a mutant defective in both glycolysis and pentose phosphate pathway builds up excessive G1P, which was suggested to inhibit an early PG precursor step, resulting in cell lysis (34). However, this observation was never

299 followed up mechanistically. *E. coli* strains with a defective *pgi* experience significant
300 sugar-phosphate stress, resulting in post-transcriptional regulation of *ptsG* to reduce
301 sugar intake (38). While G6P levels are elevated in *Δpgi* backgrounds in *E. coli*, there is
302 no observable cell-wall damage, and toxicity appears to be due to diversion of resources
303 from glycolysis, rewiring of metabolism and possibly redox imbalance stress (35, 36, 39–
304 41). The reduced glucose phosphate toxicity *in E. coli* may be due to a more enhanced
305 flux into the pentose-phosphate pathway in this species, which could in principle efficiently
306 remove G6P (41). Additionally, *E. coli* is known to have a robust glucose-phosphate stress
307 response system regulated by small RNA molecule SgrS and its activator protein, SgrR
308 (24, 42, 43). SgrS controls the excessive import of glucose through the PTS system by
309 modulating *ptsG*. While *V. cholerae* encodes an SgrR homolog, the small RNA SgrS has
310 not been identified.

311

312 Our data clearly show that sugar phosphate toxicity can directly contribute to cell
313 envelope defects. While we do not have direct evidence of the specific mode of inhibition,
314 our genetic, biochemical and modeling data point to competitive inhibition of GlmU by
315 G1P, which could be explained by the similarity in structure between G1P and GlmU's
316 natural substrate GlcN-1P (**Fig. 7**). Additionally, if G1P is targeting the acetyltransferase
317 domain, the alleviation experienced by addition of GlcNAc makes sense, as the external
318 GlcNAc would readily be converted to first GlcN6-P and then GlcN-1P. More GlcN-1P
319 would outcompete the G1P and restore GlmU functionality.

320

These findings more broadly shed light on the importance of central metabolism as a potential source of novel antibiotic targets. GlmU is a well conserved protein among highly relevant pathogens, most notably *Mycobacterium tuberculosis*. There have been extensive studies exploring the potential for GlmU as an anti-TB drug target, but little has been explored in other bacteria. Some studies have identified high throughput methods and computational models for drug screening against GlmU (44–49), while others have investigated the effect of depleting GlmU in infection models, mimicking the potential effects an inhibitor might have (50–55). In principle, UDP-GlcNAc biosynthesis serves as an ideal drug target, as it is required for not only PG, but also LPS biosynthesis. By designing targets for novel antibiotics that disrupt more than one biochemical pathway, resistance and mutations leading to reduced efficiency are less likely to occur.

Methods and Materials

Bacterial Strains and Growth Conditions

All *V. cholerae* strains used in this study are derivatives of *V. cholerae* El Tor strain N16961 and summarized in Table S1. *V. cholerae* was grown on Luria-Bertani (lysogeny broth) (LB) medium (for a 1 L bottle, 10 g Casein peptone, 5 g yeast extract, 10 g NaCl, and 12 g agar, all from Fischer Bioreagents) at 30°C or in M9 minimal medium (for a 1 L bottle, 15 g agar, 200 mL 5x M9 salts (for a 1 L bottle, 35 g Na 2 HPO 4 •7H 2 O, 15 g KH 2 PO 4 , 2.5 g NaCl, 5 g NH 4 Cl), 0.5 mL 1M MgSO 4, 0.1 mL 1M CaCl 2, and 1 mL FeCl 3 /citric acid) at 37°C; 200 µg/mL of streptomycin was also added (N16961 is streptomycin resistant). Where applicable, growth media were supplemented with 0.2% glucose (w/v),

343 0.2% casamino acids (w/v), or 0.2% GlcNAc (w/v). All other carbon sources were also
344 0.2% (w/v).
345
346 For growth dynamic experiments, overnight cultures were diluted 100-fold into 1 mL
347 growth media + streptomycin. 200µL of this seed stock were added to wells in a 100-well
348 honeycomb and incubated in a Bioscreen growth plate reader (Growth Curves America)
349 at 37°C with random shaking at maximum amplitude, and OD 600 recorded at 10 min
350 intervals.
351
352 Plasmid and strain construction.
353 Oligonucleotides used in this study are summarized in Table S2. *E. coli* MFDλpir (a
354 diaminopimelic acid [DAP] auxotroph) or SM10 λpir was used for conjugation into *V.*
355 *cholerae*, for gene deletions and overexpression plasmids respectively (56).
356 Overexpression strains were created using the chromosomal integration plasmid
357 pTD101, a derivative of pJL1 containing lacIq and a multiple-cloning site under the control
358 of the IPTG (isopropyl-β-d-thiogalactopyranoside)-inducible Ptac promoter, or
359 pHL100mob, a non-integrative high copy number plasmid also inducible through
360 IPTG(57). pTD101 integrates into the native *V. cholerae* lacZ (*vc2338*) locus. Genes for
361 complementation experiments were amplified from N16961 genomic DNA (58),
362 introducing a strong consensus ribosome-binding site (RBS) (AGGAGA), and cloned
363 using Gibson assembly. Plasmids were colony PCR verified using primers 1 and 2
364 (pTD101) or 5 and 6 (pHL100mob). Gene deletions were constructed using the pTOX5
365 cmR/msqR allelic exchange system (59). In short, 500-bp regions flanking the gene to be

366 deleted were amplified from N16961 genomic DNA by PCR and cloned into the suicide
367 vector using Gibson assembly (60). Plasmids were colony PCR verified using primers 3
368 and 4. All plasmids were Sanger sequence verified before conjugation.
369
370 Conjugation into *V. cholerae* was performed by mixing overnight cultures 1:1 (100 µL
371 donor plus 100 µL recipient) in 800 µL fresh LB, followed by pelleting (7,000 rpm, 2 min)
372 and resuspending in 100 µL LB. The mixture was then spotted onto LB agar (with 600 µM
373 DAP for E. coli MFDλpir growth) and incubated for 4 hr (overnight for pTOX5 deletions)
374 at 37°C. Selection for single-crossover mutants was then achieved by streaking the
375 mating mixture on either streptomycin (200 µg/mL) plus carbenicillin (100 µg/mL)
376 (pTD101), streptomycin (200 µg/mL) plus kanamycin (50 µg/mL) (pHL100mob), or
377 streptomycin (200 µg/mL) plus chloramphenicol (100 µg/mL) and 600 µM DAP for pTOX5
378 and incubating overnight at 37°C.
379
380 For pTD101 insertion, carbenicillin-resistant mutants were counterselected on salt-free
381 LB supplemented with 10% sucrose and X-Gal (5-bromo-4-chloro-3-indolyl-β-d-
382 galactopyranoside) (120µg/mL) and grown at ambient temperature for two days. White
383 colonies (indicating a disrupted lacZ) were isolated, and PCR-verified using primers 23
384 and 24. For pTox-mediated recombination, chloramphenicol-resistant colonies were
385 counter selected on M9 minimal medium containing 2% (vol/vol) rhamnose at 30°C for 18
386 hr. Deletions were verified by PCR using flanking and internal primers and verified with
387 whole-genome sequencing.
388

389 Cell Viability Assay and Glucose Time-dependent Killing Assay

390 To test cell viability, overnight cultures were added to sterile 1X PBS for serial dilution
391 from 1:10 to $1:10^7$. 5 µL of overnight cultures and diluted cultures were spotted for
392 CFU/mL on different media plates, as described in the figure legend. Dried plates were
393 then incubated at 37°C (M9 agar) overnight and counted the next day. For glucose
394 concentration-dependent experiments, strains were grown overnight in M9 + 0.2%
395 casamino acids at 37°C. The following day, the cultures were diluted 1:1000 into fresh M9
396 + 0.2% casamino acids and incubated at 37°C for 3 hours. Then various concentrations
397 of glucose were added to the media and incubated for another 3 hours at 37°C, then
398 serially diluted onto M9 agar + 0.2% casamino acids and left overnight at 37°C. CFU/mL
399 were counted the next day. For microscopy, strains were grown as previously described
400 then imaged without fixation on M9 + 0.8% agarose pads using a Leica DMi8 inverted
401 microscope.

402

403 Antibiotic Sensitivity Assay

404 For zone of inhibition assays, a lawn of overnight cultures (100 µL) was spread on an LB
405 agar plate with or without 0.2% GlcNAc and allowed to dry for 15 min. 10 µL of antibiotic
406 solutions (100 mg/mL PenG or 100mg/mL carbenicillin) were placed on Thermo Scientific
407 Oxoid Antimicrobial Susceptibility Test filter disks (6 mm, product code: 10609174) onto
408 the agar surface and incubated at 30°C overnight before measurements.

409

410 Metabolomics

Three biological replicates were grown in M9 + 0.2% casamino acids overnight at 37°C. 1mL of culture was pelleted (2 min, 7000 rpm) and washed with M9 media. The cultures were then added 1:50 into 5mL of M9 + 0.2% casamino acids and incubated at 37°C for 3 hours. Following incubation, either 0.2% glucose or 0.2% glucose and 0.2% GlcNAc were added to the tubes and incubated for an additional hour at 37°C. After treatment, 2 mL of sample were taken per condition and pelleted at 7000 rpm for 2 min. The supernatant was removed, and the cell material pellet was flash frozen with liquid nitrogen. 200 µL of cold 80% methanol was then added to the pellets. Pellets were stored at -80°C. These pellets were lysed and 3 µl samples were analyzed using Agilent InfinityLab Poroshell 120 HILIC-Z (Agilent 683775-924). The chromatographic separation employed two solvent phases: Solvent A (water + 10 mM NH4OAc + 5 mM InfinityLab Deactivator Additive, pH 9, adjusted with NH4OH) and Solvent B (85% ACN + 10 mM NH4OAc + 5 mM InfinityLab Deactivator Additive, pH 9, adjusted with NH4OH). The gradient program consisted of 0-2 min (96% B), 5.5-8.5 min (88% B), 9-14 min (86% B), 17 min (82% B), 23-24 min (65% B), 24.5-26 min (96% B), and a 10-minute end-run at 96% B. Mass spectrometry was performed using an Agilent 6230 Time of Flight (TOF) mass spectrometer with an Agilent Jet Stream electrospray ionization (ESI) source in negative mode. Data analysis involved peak visualization and confirmation using Profinder 8.0 (Agilent) software and a pathway-specific, manually curated database. Standard metabolites were included in each run for retention time matching and verification. Heatmaps were generated using Prism, with averaged peak heights normalized to the control casamino acids condition.

Protein Purification

V. cholerae's GlmU gene was amplified from N16961 gDNA and cloned into pET28a downstream of 6xHis-SUMO Tag (61). Plasmids were verified by Sanger sequencing. *E. coli* BL21 (DE3) (Novagen) was transformed with the resulting recombinant plasmid (pET28a-GlmU). Overnight cultures (10 mL) were used to inoculate 1L of LB with kanamycin (50 µg/mL) and incubated at 37°C with vigorous shaking (220 RPM) until they reached an OD600 between 0.6 and 0.8. Cultures were induced with 1mM IPTG at 18°C and 180 RPM overnight. Harvested cells were pelleted and resuspended in 15 mL of cold purification buffer (20mM Tris pH 7.5, 150 mM NaCl), and lysed by sonication. Lysates were cleared by centrifugation at 31,000g for 40 minutes at 4°C, and loaded onto a HisPur cobalt column (Thermo Scientific; Catalog No. 89964) and washed multiple times with purification buffer until protein was undetectable in the flowthrough by the Bradford reagent. The bead slurry was then transferred to a 5 mL microtube with 60 µL of ULP1 Sumo protease and digested overnight at 4°C rotating. Protein was eluted the next day with 20 mL of purification buffer. Samples were analyzed by SDS-page with Coomassie blue stain and then Concentrated with a 30KD Amicon concentrator (Millipore) to 5 mL. Concentrated samples were then measured using Nanodrop.

In vitro GlmU biochemistry

Reaction design was taken from (50). In summary, GlmU reaction substrates included GlcN-1P (5mM), UTP (5mM), and Acetyl-CoA (5mM). substrates were added to a 1.5mL Eppendorf tube with 5µL of 10x Reaction Buffer (50mM Tris–HCl, pH 7.5, 5 and 5mM $MgCl_2$). A dilution series of G1P inhibitors were added (0mM – 250mM) and then

457 purified $GlmU^{VC}$ was added at 2 µM, for a total volume of 50µL. The tubes were
458 incubated at 30°C for 30min. Equal volumes of 40:40:20 (Acn: MeOH:H_2O) solution
459 was added to stop the biochemical reaction. The tubes were then centrifuged for 10min
460 at 15,000rpm. Half of the volume was added to a new tube and mixed with equal
461 volumes of LC-MS Solution B. These tubes were centrifuged at 4°C, 8min, at
462 15,000rpm. 25µL of supernatant was added to the LC-MS autosampler vials and 2 µl
463 sample volume were resolved on a Diamond Hydride Column using a 1260 Infinity II
464 high-performance liquid chromatography (LC) system (Agilent) coupled with an Agilent
465 Accurate-Mass 6230 TOF-Mass Spectrometer (MS) operating in negative mode. Two
466 liquid phases (i) solvent A: H_2O + 0.2% formic acid and (ii) solvent B: Acetonitrile +
467 0.2% formic acid were used at 0.4 ml/ min with the following gradients: 85% B, 0-2min;
468 80% B, 3-5min; 75% B, 6-7 min; 70% B, 8-9 min; 50% B, 10-11 min; 20% B, 11-14 min;
469 5% B, 14-24 min and 10 min of 85% B for the re-equilibration. Results were collected
470 on Agilent 6230 TOF-MS with ESI source. Profinder 8.0 (Agilent) was used for the peak
471 abundance measurement. Final metabolites were verified by comparing retention
472 times and mass-to-charge (m/z) ratios with respective standards for each substrate
473 and product. Absolute and relative counts were calculated and plotted on GraphPad
474 Prism software.

475

476 Molecular Modeling

477 Interactions between GlmU, glucosamine-1-P, and glucose-1-P were modeled using Chai
478 Discovery (https://www.chaidiscovery.com/blog/introducing-chai-1). We input the amino
479 acid sequence code for VCH GlmU, from UniProt (Q9KNH7) as the protein input x3. We

480 then uploaded the SMILES for either glucosamine-1P or glucose-1P (PubChem).
481 Confidence scores (pTM and ipTM) were automatically generated during this analysis.
482 Each resulting model was visualized using PyMol. Polar interactions to adjacent amino
483 acids were identified and measured in PyMol. Pairwise structural alignments were
484 performed in PyMol and RMSD values were automatically generated during this analysis.
485 Sequence alignments and analysis were performed using UniProt
486 (https://www.uniprot.org/align).
487

488 **Acknowledgements**

489 MRK is supported by the National Institutes of Health and National Institute of Allergy
490 and Infectious Diseases Award T32AI145821. Tolerance research in the Dörr lab is
491 supported by NIH R01 AI143704. The Rhee lab is funded by NIH R25 AI140472.
492

493 **References**

494 1. Huemer M, Shambat SM, Brugger SD, Zinkernagel AS. 2020. Antibiotic resistance and
495 persistence—Implications for human health and treatment perspectives. EMBO
496 Reports 21.

497 2. CDC. 2022. The biggest antibiotic-resistant threats in the U.S. Centers for Disease
498 Control and Prevention. https://www.cdc.gov/drugresistance/biggest-threats.html.
499 Retrieved 21 December 2023.

500 3. Brauner A, Fridman O, Gefen O, Balaban NQ. 2016. Distinguishing between resistance,
501 tolerance and persistence to antibiotic treatment. Nat Rev Microbiol 14:320–330.

4. Balaban NQ, Helaine S, Lewis K, Ackermann M, Aldridge B, Andersson DI, Brynildsen MP, Bumann D, Camilli A, Collins JJ, Dehio C, Fortune S, Ghigo J-M, Hardt W-D, Harms A, Heinemann M, Hung DT, Jenal U, Levin BR, Michiels J, Storz G, Tan M-W, Tenson T, Van Melderen L, Zinkernagel A. 2019. Definitions and guidelines for research on antibiotic persistence. Nat Rev Microbiol 17:441–448.

5. Dörr T. 2021. Understanding tolerance to cell wall–active antibiotics. Annals of the New York Academy of Sciences 1496:35–58.

6. Darnell RL, Paxie O, Todd Rose FO, Morris S, Krause AL, Monk IR, Smith MJB, Stinear TP, Cook GM, Gebhard S. 2022. Chapter Two - Antimicrobial tolerance and its role in the development of resistance: Lessons from enterococci, p. 25–65. *In* Poole, RK, Kelly, DJ (eds.), Advances in Microbial Physiology. Academic Press.

7. Levin-Reisman I, Ronin I, Gefen O, Braniss I, Shoresh N, Balaban NQ. 2017. Antibiotic tolerance facilitates the evolution of resistance. Science 355:826–830.

8. Kawai Y, Mercier R, Mickiewicz K, Serafini A, Sório de Carvalho LP, Errington J. 2019. Crucial role for central carbon metabolism in the bacterial L-form switch and killing by β-lactam antibiotics. 10. Nat Microbiol 4:1716–1726.

9. Keller MR, Dörr T. 2023. Chapter Four - Bacterial metabolism and susceptibility to cell wall-active antibiotics, p. 181–219. *In* Poole, RK, Kelly, DJ (eds.), Advances in Microbial Physiology. Academic Press.

10. Keller M, Han X, Dörr T. 2023. Disrupting Central Carbon Metabolism Increases β-Lactam Antibiotic Susceptibility in Vibrio cholerae. Journal of Bacteriology 205:e00476-22.

11. Stokes JM, Lopatkin AJ, Lobritz MA, Collins JJ. 2019. Bacterial Metabolism and Antibiotic Efficacy. Cell Metab 30:251–259.

12. Wong F, Stokes JM, Bening SC, Vidoudez C, Trauger SA, Collins JJ. 2022. Reactive metabolic byproducts contribute to antibiotic lethality under anaerobic conditions. Mol Cell 82:3499-3512.e10.

13. Lobritz MA, Andrews IW, Braff D, Porter CBM, Gutierrez A, Furuta Y, Cortes LBG, Ferrante T, Bening SC, Wong F, Gruber C, Bakerlee CW, Lambert G, Walker GC, Dwyer DJ, Collins JJ. 2022. Increased energy demand from anabolic-catabolic processes drives β-lactam antibiotic lethality. Cell Chem Biol 29:276-286.e4.

14. Ducker GS, Rabinowitz JD. 2017. One-Carbon Metabolism in Health and Disease. Cell Metab 25:27–42.

15. Noor E, Eden E, Milo R, Alon U. 2010. Central Carbon Metabolism as a Minimal Biochemical Walk between Precursors for Biomass and Energy. Molecular Cell 39:809–820.

16. Westfall CS, Levin PA. 2018. Comprehensive analysis of central carbon metabolism illuminates connections between nutrient availability, growth rate, and cell morphology in Escherichia coli. PLoS Genet 14:e1007205.

17. Judge A, Dodd MS. 2020. Metabolism. Essays in Biochemistry 64:607–647.

18. Cross T, Ransegnola B, Shin J-H, Weaver A, Fauntleroy K, VanNieuwenhze MS, Westblade LF, Dörr T. 2019. Spheroplast-Mediated Carbapenem Tolerance in Gram-Negative Pathogens. Antimicrobial Agents and Chemotherapy 63:e00756-19.

19. Dörr T, Alvarez L, Delgado F, Davis BM, Cava F, Waldor MK. 2016. A cell wall damage response mediated by a sensor kinase/response regulator pair enables beta-lactam tolerance. PNAS 113:404–409.

20. Weaver AI, Murphy SG, Umans BD, Tallavajhala S, Onyekwere I, Wittels S, Shin J-H, VanNieuwenhze M, Waldor MK, Dörr T. 2018. Genetic Determinants of Penicillin Tolerance in Vibrio cholerae. Antimicrob Agents Chemother 62.

21. Dörr T, Davis BM, Waldor MK. 2015. Endopeptidase-Mediated Beta Lactam Tolerance. PLOS Pathogens 11:e1004850.

22. Paradis-Bleau C, Kritikos G, Orlova K, Typas A, Bernhardt TG. 2014. A Genome-Wide Screen for Bacterial Envelope Biogenesis Mutants Identifies a Novel Factor Involved in Cell Wall Precursor Metabolism. PLoS Genet 10:e1004056.

23. Sezonov G, Joseleau-Petit D, D'Ari R. 2007. Escherichia coli physiology in Luria-Bertani broth. J Bacteriol 189:8746–8749.

558 24. Richards GR, Patel MV, Lloyd CR, Vanderpool CK. 2013. Depletion of Glycolytic
559 Intermediates Plays a Key Role in Glucose-Phosphate Stress in Escherichia coli. J
560 Bacteriol 195:4816–4825.

561 25. Yadav V, Panilaitis B, Shi H, Numuta K, Lee K, Kaplan DL. 2011. N-acetylglucosamine 6-
562 Phosphate Deacetylase (nagA) Is Required for N-acetyl Glucosamine Assimilation in
563 Gluconacetobacter xylinus. PLOS ONE 6:e18099.

564 26. Craggs PD, Mouilleron S, Rejzek M, de Chiara C, Young RJ, Field RA, Argyrou A, de
565 Carvalho LPS. 2018. The Mechanism of Acetyl Transfer Catalyzed by Mycobacterium
566 tuberculosis GlmU. Biochemistry 57:3387–3401.

567 27. Abramson J, Adler J, Dunger J, Evans R, Green T, Pritzel A, Ronneberger O, Willmore L,
568 Ballard AJ, Bambrick J, Bodenstein SW, Evans DA, Hung C-C, O'Neill M, Reiman D,
569 Tunyasuvunakool K, Wu Z, Žemgulytė A, Arvaniti E, Beattie C, Bertolli O, Bridgland A,
570 Cherepanov A, Congreve M, Cowen-Rivers AI, Cowie A, Figurnov M, Fuchs FB, Gladman
571 H, Jain R, Khan YA, Low CMR, Perlin K, Potapenko A, Savy P, Singh S, Stecula A,
572 Thillaisundaram A, Tong C, Yakneen S, Zhong ED, Zielinski M, Žídek A, Bapst V, Kohli P,
573 Jaderberg M, Hassabis D, Jumper JM. 2024. Accurate structure prediction of
574 biomolecular interactions with AlphaFold 3. Nature 630:493–500.

575 28. Chai Discovery. https://www.chaidiscovery.com/blog/introducing-chai-1. Retrieved 30
576 September 2024.

29. EMBL-EBI. Confidence scores in AlphaFold-Multimer | AlphaFold. https://www.ebi.ac.uk/training/online/courses/alphafold/inputs-and-outputs/evaluating-alphafolds-predicted-structures-using-confidence-scores/confidence-scores-in-alphafold-multimer/. Retrieved 21 October 2024.

30. Olsen LR, Vetting MW, Roderick SL. 2007. Structure of the E. coli bifunctional GlmU acetyltransferase active site with substrates and products. Protein Science 16:1230–1235.

31. Englesberg E, Anderson RL, Weinberg R, Lee N, Hoffee P, Huttenhauer G, Boyer H. 1962. l-ARABINOSE-SENSITIVE, l-RIBULOSE 5-PHOSPHATE 4-EPIMERASE-DEFICIENT MUTANTS OF ESCHERICHIA COLI. Journal of Bacteriology 84:137–146.

32. Irani MH, Maitra PK. 1977. Properties of Escherichia coli Mutants Deficient in Enzymes of Glycolysis. Journal of Bacteriology 132:398–410.

33. Kadner RJ, Murphy GP, Stephens CM. 1992. Two mechanisms for growth inhibition by elevated transport of sugar phosphates in Escherichia coli. Microbiology 138:2007–2014.

34. Prasad C, Freese E. 1974. Cell lysis of Bacillus subtilis caused by intracellular accumulation of glucose-1-phosphate. J Bacteriol 118:1111–1122.

35. Fraenkel DG. 1968. Selection of Escherichia coli Mutants Lacking Glucose-6-Phosphate Dehydrogenase or Gluconate-6-Phosphate Dehydrogenase. Journal of Bacteriology 95:1267–1271.

36. Fraenkel DG. 1968. The Accumulation of Glucose 6-Phosphate from Glucose and Its Effect in an *Escherichia coli* Mutant Lacking Phosphoglucose Isomerase and Glucose 6-Phosphate Dehydrogenase. Journal of Biological Chemistry 243:6451–6457.

37. Boulanger EF, Sabag-Daigle A, Thirugnanasambantham P, Gopalan V, Ahmer BMM. 2021. Sugar-Phosphate Toxicities. Microbiology and Molecular Biology Reviews 85:e00123-21.

38. Kimata K, Tanaka Y, Inada T, Aiba H. 2001. Expression of the glucose transporter gene, ptsG, is regulated at the mRNA degradation step in response to glycolytic flux in Escherichia coli. EMBO J 20:3587–3595.

39. Usui Y, Hirasawa T, Furusawa C, Shirai T, Yamamoto N, Mori H, Shimizu H. 2012. Investigating the effects of perturbations to pgi and eno gene expression on central carbon metabolism in Escherichia coli using 13 C metabolic flux analysis. Microbial Cell Factories 11:87.

40. Long CP, Gonzalez JE, Feist AM, Palsson BO, Antoniewicz MR. 2018. Dissecting the genetic and metabolic mechanisms of adaptation to the knockout of a major metabolic enzyme in Escherichia coli. Proc Natl Acad Sci U S A 115:222–227.

41. McCloskey D, Xu S, Sandberg TE, Brunk E, Hefner Y, Szubin R, Feist AM, Palsson BO. 2018. Multiple Optimal Phenotypes Overcome Redox and Glycolytic Intermediate Metabolite Imbalances in Escherichia coli pgi Knockout Evolutions. Applied and Environmental Microbiology 84:e00823-18.

617 42. Wadler CS, Vanderpool CK. 2007. A dual function for a bacterial small RNA: SgrS
618 performs base pairing-dependent regulation and encodes a functional polypeptide.
619 Proceedings of the National Academy of Sciences 104:20454–20459.

620 43. Vanderpool CK, Gottesman S. 2004. Involvement of a novel transcriptional activator
621 and small RNA in post-transcriptional regulation of the glucose phosphoenolpyruvate
622 phosphotransferase system. Molecular Microbiology 54:1076–1089.

623 44. Chen C, Han X, Yan Q, Wang C, Jia L, Taj A, Zhao L, Ma Y. 2019. The Inhibitory Effect of
624 GlmU Acetyltransferase Inhibitor TPSA on Mycobacterium tuberculosis May Be
625 Affected Due to Its Methylation by Methyltransferase Rv0560c. Front Cell Infect
626 Microbiol 9:251.

627 45. Tran AT, Wen D, West NP, Baker EN, Britton WJ, Payne RJ. 2013. Inhibition studies on
628 Mycobacterium tuberculosis N-acetylglucosamine-1-phosphate uridyltransferase
629 (GlmU). Org Biomol Chem 11:8113–8126.

630 46. Jia J, Zheng M, Zhang C, Li B, Lu C, Bai Y, Tong Q, Hang X, Ge Y, Zeng L, Zhao M, Song F,
631 Zhang H, Zhang L, Hong K, Bi H. 2023. Killing of Staphylococcus aureus persisters by a
632 multitarget natural product chrysomycin A. Science Advances 9:eadg5995.

633 47. Mehra R, Rani C, Mahajan P, Vishwakarma RA, Khan IA, Nargotra A. 2016.
634 Computationally Guided Identification of Novel Mycobacterium tuberculosis GlmU
635 Inhibitory Leads, Their Optimization, and in Vitro Validation. ACS Comb Sci 18:100–116.

636 48. Rani C, Mehra R, Sharma R, Chib R, Wazir P, Nargotra A, Khan IA. 2015. High-throughput
637 screen identifies small molecule inhibitors targeting acetyltransferase activity of
638 *Mycobacterium tuberculosis* GlmU. Tuberculosis 95:664–677.

639 49. Pereira MP, Blanchard JE, Murphy C, Roderick SL, Brown ED. 2009. High-Throughput
640 Screening Identifies Novel Inhibitors of the Acetyltransferase Activity of Escherichia coli
641 GlmU. Antimicrob Agents Chemother 53:2306–2311.

642 50. Soni V, Upadhayay S, Suryadevara P, Samla G, Singh A, Yogeeswari P, Sriram D,
643 Nandicoori VK. 2015. Depletion of M. tuberculosis GlmU from Infected Murine Lungs
644 Effects the Clearance of the Pathogen. PLoS Pathog 11:e1005235.

645 51. Soni V, Suryadevara P, Sriram D, Kumar S, Nandicoori VK, Yogeeswari P, OSDD
646 Consortium. 2015. Structure-based design of diverse inhibitors of Mycobacterium
647 tuberculosis N-acetylglucosamine-1-phosphate uridyltransferase: combined
648 molecular docking, dynamic simulation, and biological activity. J Mol Model 21:174.

649 52. Mochalkin I, Lightle S, Narasimhan L, Bornemeier D, Melnick M, VanderRoest S,
650 McDowell L. 2008. Structure of a small-molecule inhibitor complexed with GlmU from
651 Haemophilus influenzae reveals an allosteric binding site. Protein Sci 17:577–582.

652 53. Sharma R, Khan IA. 2017. Mechanism and Potential Inhibitors of GlmU: A Novel Target
653 for Antimicrobial Drug Discovery. Curr Drug Targets 18:1587–1597.

654 54. Sharma R, Lambu MR, Jamwal U, Rani C, Chib R, Wazir P, Mukherjee D, Chaubey A,
655 Khan IA. 2016. Escherichia coli N-Acetylglucosamine-1-Phosphate-

Uridyltransferase/Glucosamine-1-Phosphate-Acetyltransferase (GlmU) Inhibitory Activity of Terreic Acid Isolated from Aspergillus terreus. J Biomol Screen 21:342–353.

55. Palathoti N, Azam MA. GlmU Inhibitors as Promising Antibacterial Agents: A Review. Mini-Reviews in Medicinal Chemistry 23:343–360.

56. Ferrières L, Hémery G, Nham T, Guérout A-M, Mazel D, Beloin C, Ghigo J-M. 2010. Silent Mischief: Bacteriophage Mu Insertions Contaminate Products of Escherichia coli Random Mutagenesis Performed Using Suicidal Transposon Delivery Plasmids Mobilized by Broad-Host-Range RP4 Conjugative Machinery. Journal of Bacteriology 192:6418–6427.

57. Mett H, Bracha R, Mirelman D. 1980. Soluble nascent peptidoglycan in growing Escherichia coli cells. J Biol Chem 255:9884–9890.

58. Heidelberg JF, Eisen JA, Nelson WC, Clayton RA, Gwinn ML, Dodson RJ, Haft DH, Hickey EK, Peterson JD, Umayam L, Gill SR, Nelson KE, Read TD, Tettelin H, Richardson D, Ermolaeva MD, Vamathevan J, Bass S, Qin H, Dragoi I, Sellers P, McDonald L, Utterback T, Fleishmann RD, Nierman WC, White O, Salzberg SL, Smith HO, Colwell RR, Mekalanos JJ, Venter JC, Fraser CM. 2000. DNA sequence of both chromosomes of the cholera pathogen Vibrio cholerae. Nature 406:477–483.

59. Lazarus JE, Warr AR, Kuehl CJ, Giorgio RT, Davis BM, Waldor MK. 2019. A New Suite of Allelic-Exchange Vectors for the Scarless Modification of Proteobacterial Genomes. Applied and Environmental Microbiology 85:e00990-19.

676 60. Gibson DG, Young L, Chuang R-Y, Venter JC, Hutchison CA, Smith HO. 2009. Enzymatic
677 assembly of DNA molecules up to several hundred kilobases. 5. Nat Methods 6:343–
678 345.

679 61. Obando MA, Rey-Varela D, Cava F, Dörr T. 2024. Genetic interaction mapping reveals
680 functional relationships between peptidoglycan endopeptidases and
681 carboxypeptidases. PLOS Genetics 20:e1011234.

682

683

684

685 **Figures**

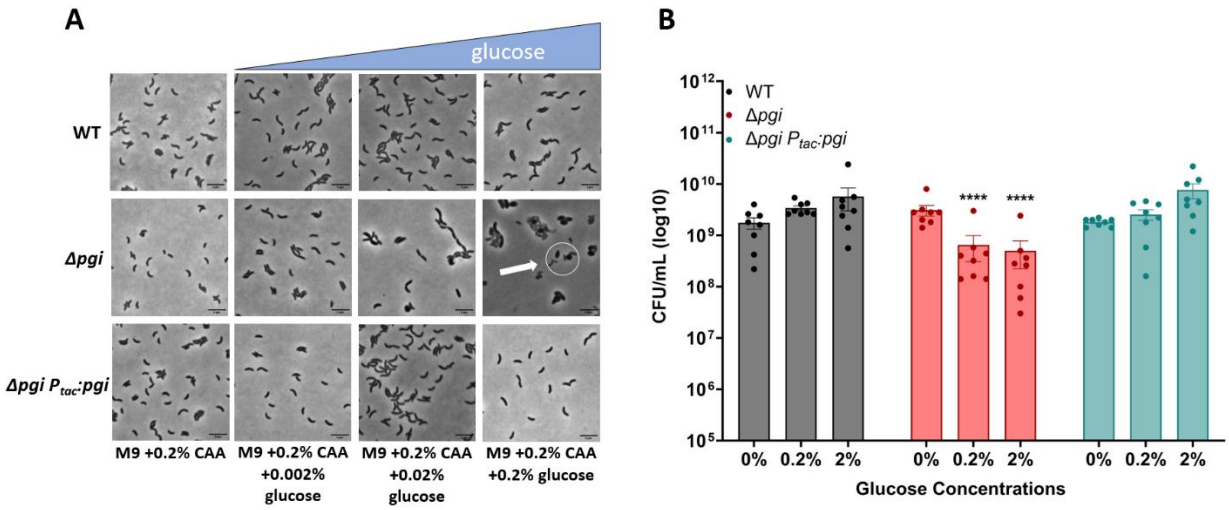

686

687 **Figure 1: Glucose toxicity in Δ*pgi*.** A) Cells were imaged after 3 hours of growth in the
688 indicated conditions. Scale bar = 5 μm. White circle indicates aberrant cell morphologies
689 B) CFU measurements from serially diluted cultures plated on M9 + 0.2% casamino acids
690 agar after 3 hours of exposure to the indicated glucose concentrations. Mean with SEM
691 plotted with 7 independent biological replicates. **=p<0.01, *** = p<0.001, ****=p<0.0001
692 (2-way ANOVA).
693

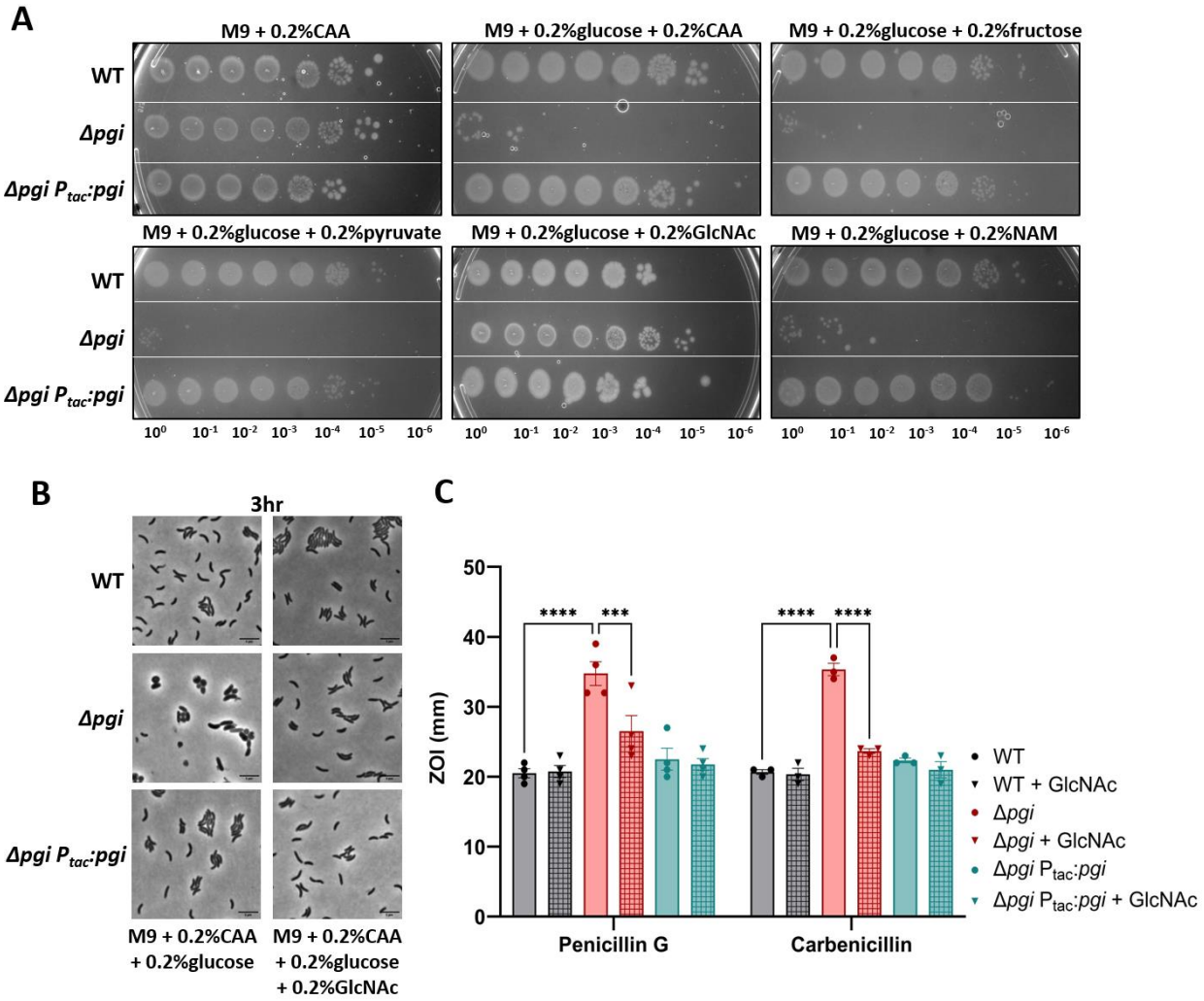

Figure 2: External GlcNAc is sole carbon source to complement Δ*pgi* in glucose. A) Serial dilutions of the indicated strains were plated on M9 minimal media supplemented with the indicated carbon sources and grown overnight at 37°C. B) The indicated mutant strains were imaged after 3 hours of growth at 37°C. Bar = 5 μm. C) Zone of inhibition measurements from a disk diffusion experiment on LB agar with or without the addition of 0.2% GlcNAc. Concentrations of the noted antibiotics are listed in Methods and Materials. Data represent at least 3 independent biological replicates; raw data points are shown with bars depicting mean with SEM. *** = p<0.001, ****=p<0.0001 (2-way ANOVA).

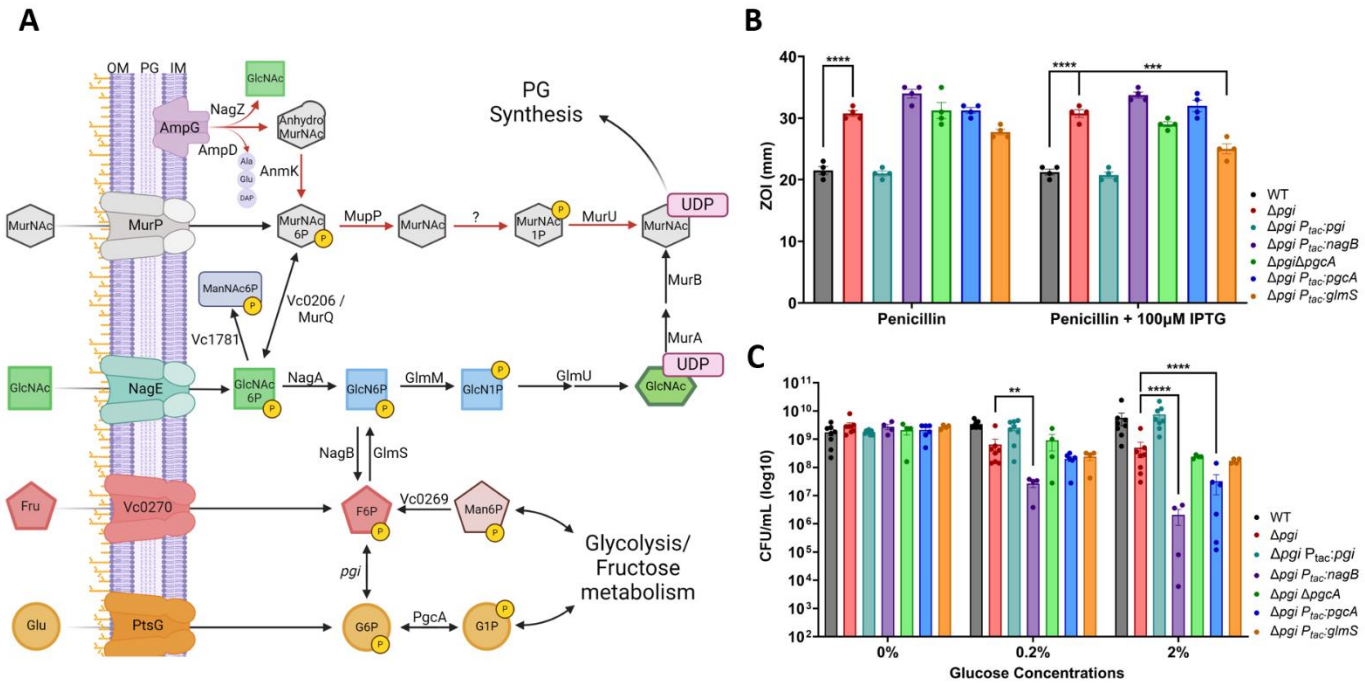

Figure 3: Genetic manipulation of biosynthesis pathways reveals an essentiality of glucosamine-6P in Δ*pgi*. A) A metabolic pathway diagram highlighting the PG recycling pathway, the conversion of glycolytic intermediates towards PG synthesis, and GlcNAc import. Glucose (Glu) can be imported through PtsG and readily converted to Glucose-6P. PgcA can also convert glucose-1P and glucose-6P interchangeably. Fructose (Fru) can be imported through *vc0270*, a member of the PTS system. Pgi interconverts G6P and F6P. Mannose-6P (Man6P) can be siphoned from central metabolism towards F6P. NagB and GlmS act as a bridge away from and towards PG synthesis, respectively. GlcNAc is imported through NagE and converted to Glucosamine-6P by NagA. GlmM and GlmU build the PG precursor UDP-GlcNAc, while MurA and MurB add some additional steps to create UDP-MurNAc. MurNAc can also be imported through MurP. As MurNAc-6P, this molecule can either be funneled back towards PG synthesis directly, through MupP, MurU and an uncharacterized enzyme, or recycled back into GlcNAc-6P by MurQ/*vc0206*. AmpG, a periplasmic PG fragment importer, can also supply internal GlcNAc from degraded cell wall products. B) Zone of inhibition data from treatment with PenG with and without overexpression induction. Statistical significance was evaluated via 2-way ANOVA from at least 5 independent replicates (raw data points shown). *** = p<0.001, ****=p<0.0001 C) Colony formation after 3 hours of glucose exposure with the indicated strains were plated on M9 + 0.2% CAA. Data for WT, Δ*pgi*, and complemented strain are reproduced from Fig.1 for comparison. Statistical significance was evaluated via log-transformed, 2-way ANOVA with 4 independent replicates (raw data points shown). *=p<0.1 **=p<0.01, *** = p<0.001, ****=p<0.0001.

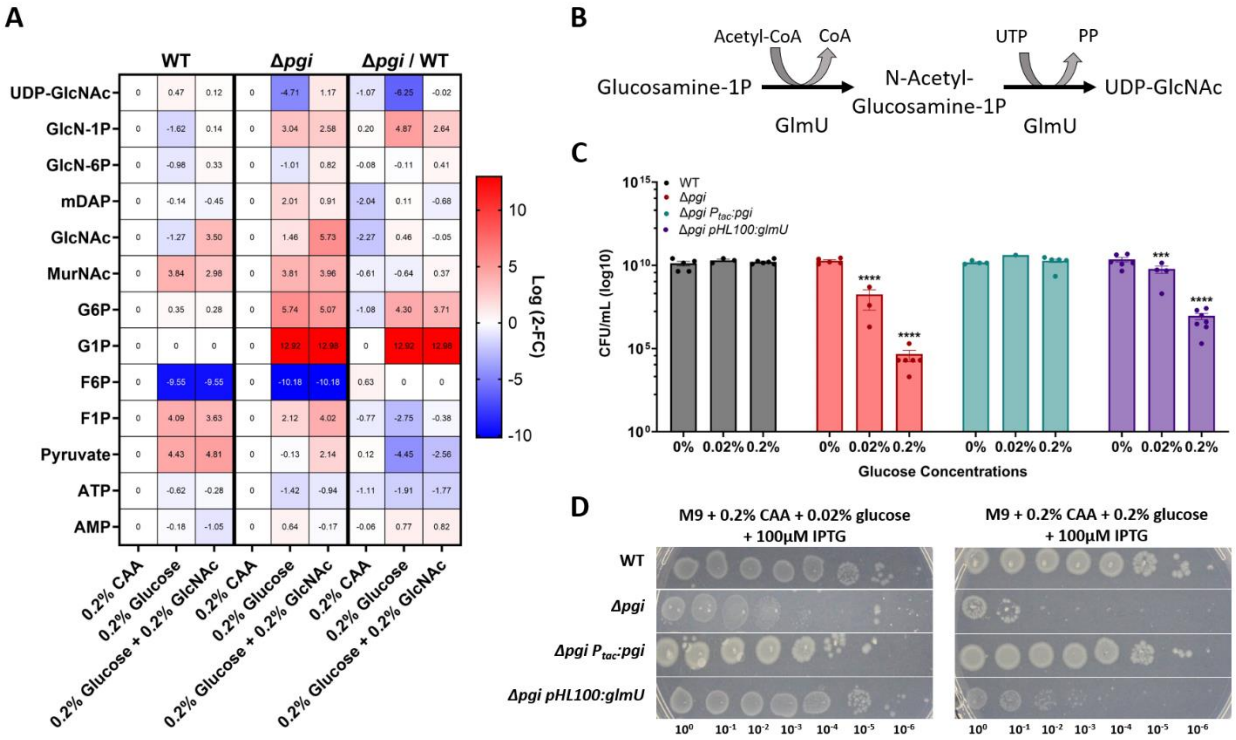

Figure 4: Targeted metabolomics of Δ*pgi* reveal bottleneck around GlmU activity. A) Heatmaps normalized to strain specific casamino acids conditions. The right column represents the change between strains in the indicated conditions. Log2 fold change is shown on the right side of the maps. B) The enzymatic reaction of GlmU. The acetyltransferase activity catalyzes N-acetylglucosamine-1P from glucosamine-1P and Acetyl-CoA. The second step is the uridyltransferase reaction which adds UDP onto GlcNAc, forming the end-product UDP-GlcNAc. C) Overnight cultures were serially diluted and spot-plated on MM agar with the indicated additions of percent glucose and 200uM IPTG. At least 4 independent replicates are presented, with raw data points and SEM. *** = p<0.001, ****=p<0.0001 (2-way ANOVA). Δ*pgi* was compared against WT values and Δ*pgi* pHL100: *glmU* was compared against Δ*pgi.* D) The indicated strains were grown overnight in M9 + casamino acids and the diluted and spot-plated on M9 agar plates containing CAA and the indicated glucose concentration.

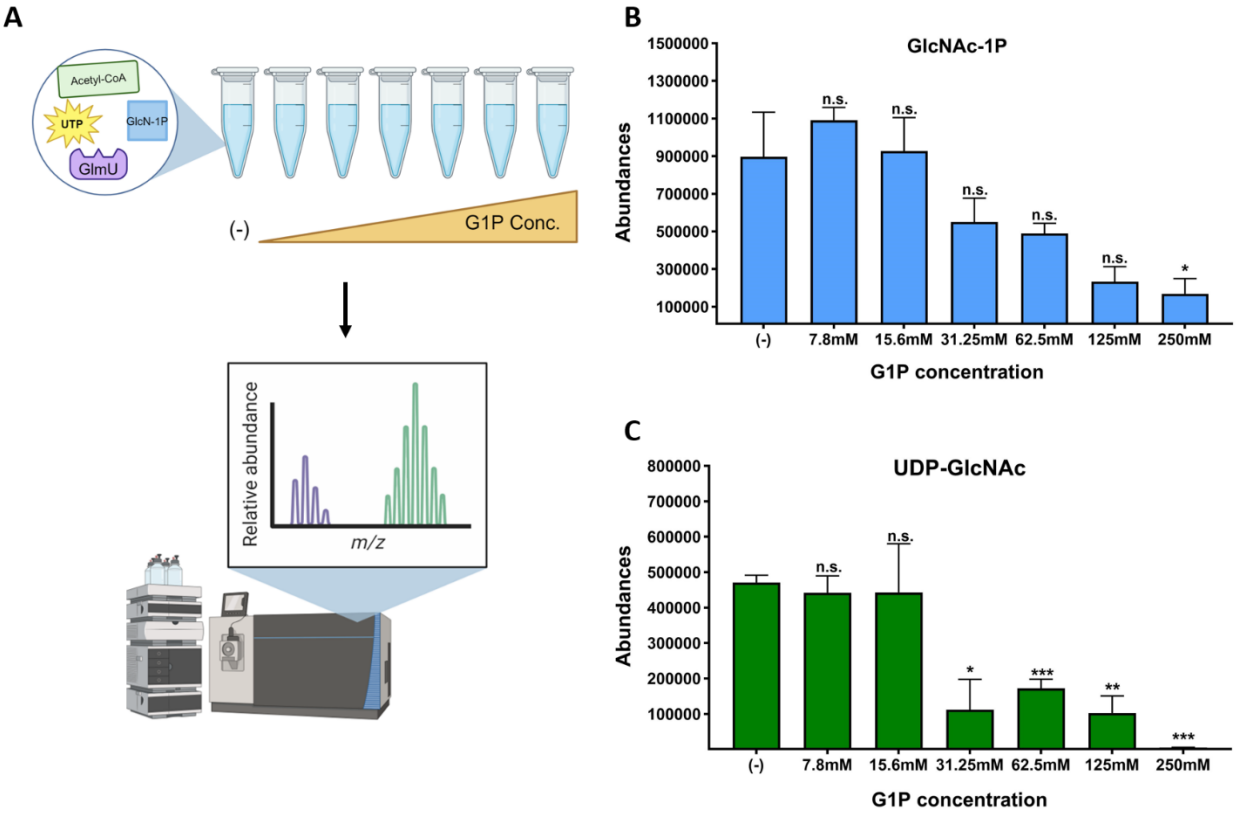

Figure 5: Glucose-1P inhibits GlmU biochemical reaction in a concentration dependent manner. A) Schematic portraying the *in vitro* biochemistry experimental design. Biochemical reaction components, UTP, Acetyl-CoA, GlcN-1P and GlmU, mixed with buffer, were added to test tubes. After incubation, the reaction was stopped and ran on the LC-MS machine. Abundance peaks were measured for the stated molecules. B) Peak values for GlcNAc-1P product from reactions with increasing glucose-1P concentrations. SEM plotted with 3 replicates. * = $p < 0.05$ (unpaired t-tests). C) Peak values for UDP-GlcNAc product from reactions with increasing glucose-1P concentrations (in mM, X-axis). Averages and SEM plotted from 3 replicates. * = $p < 0.02$, ** = $p < 0.002$, *** = $p < 0.0005$ (unpaired t-test).

A

Model	Polar interactions	Bond length (Å)	pTM	ipTM
GlmU + glucosamine-1-P	Arg 330	3.0	0.9556	0.9388
	Lys 348	3.5		
	Tyr 363	2.7, 2.9, 3.6		
	Asn 374	2.1		
	Asn 383	3.2, 3.3, 3.4		
	Lys 389	2.8, 3.0, 3.2, 3.3		
GlmU + glucose-1-P	Arg 330	3.3	0.9549	0.9376
	Lys 348	3.5		
	Asg 359	3.0		
	Tyr 363	2.6, 3.1		
	Asn 374	3.0, 3.3		
	Asn 383	2.9, 3.3, 3.4		
	Lys 389	3.1, 3.5		

B **C**

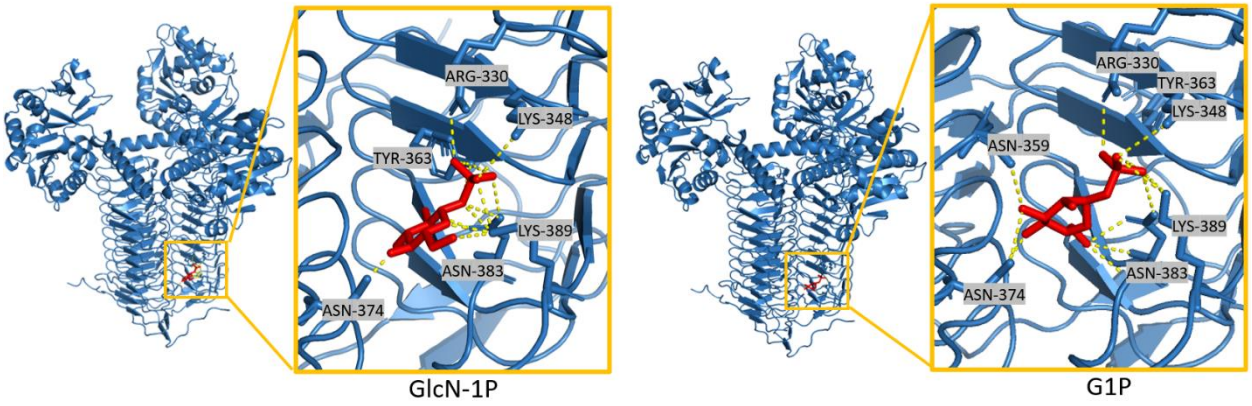

Figure 6: Molecular modeling reveals putative target site for glucose phosphate inhibition. A) Residues predicted to interact with glucosamine-1-P and glucose-1-P, Predicted Template Modeling (pTM) and Interface Predicted Template Modeling (ipTM). B) Molecular modeling of GlmU binding glucosamine-1-P (red) and the associated polar interactions. C) Molecular modeling of GlmU binding glucose-1-P (red) and the associated polar interactions.

770 **Supporting Information**

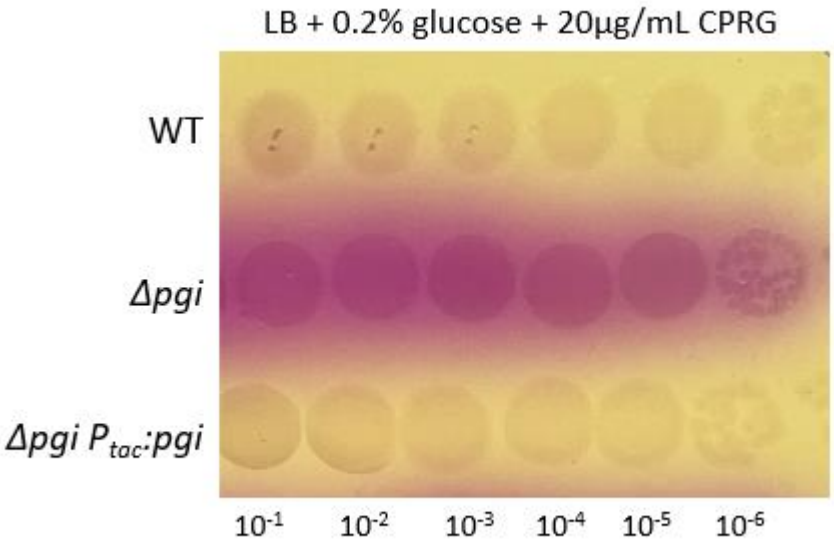

771

772 Figure S1: Enhanced lysis of a *pgi* mutant. Overnight cultures of the indicated strains
773 were plated on agar containing glucose and the lysis indicator CPRG (see text for details)
774 and imaged after 18 hours of growth.
775

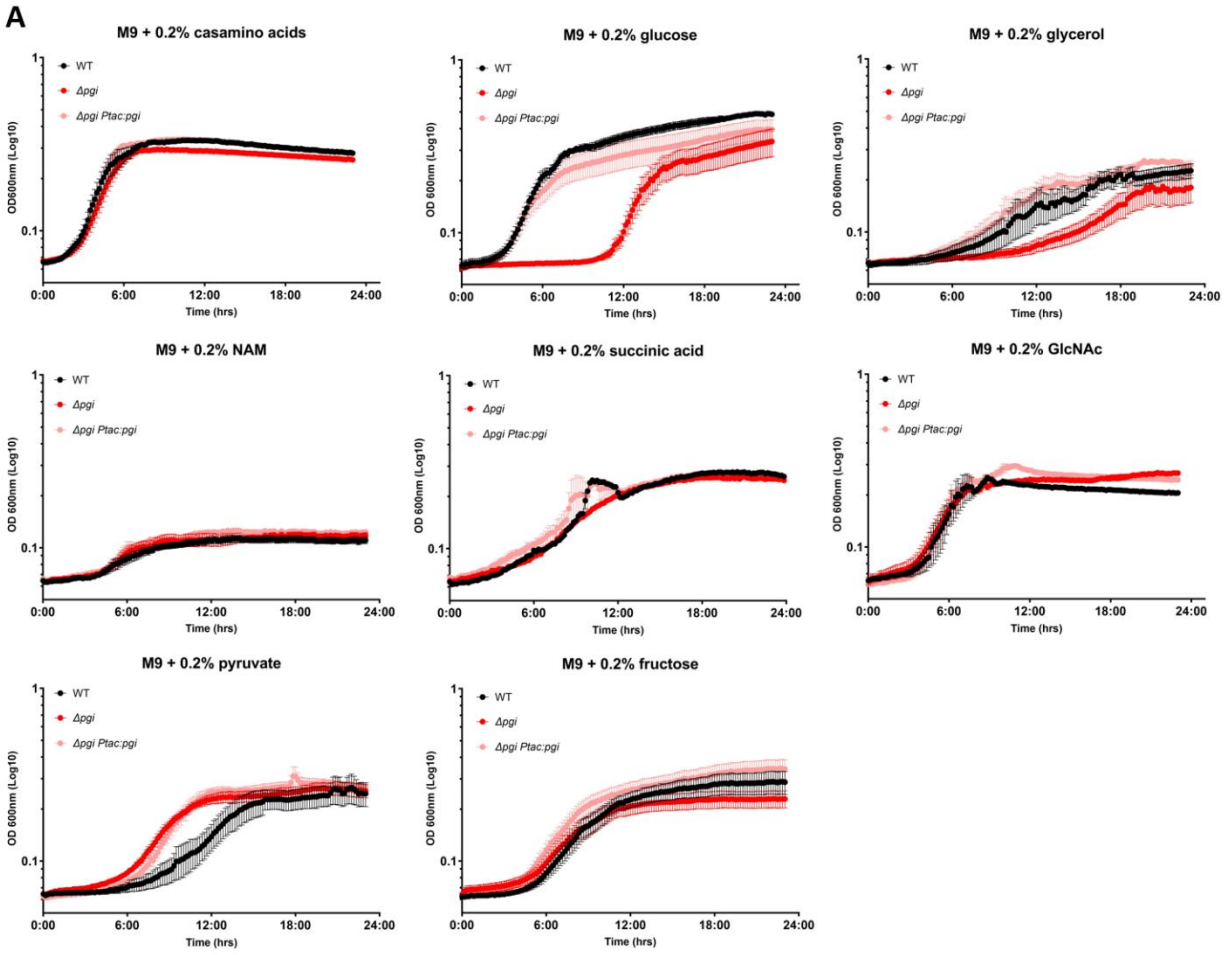

776

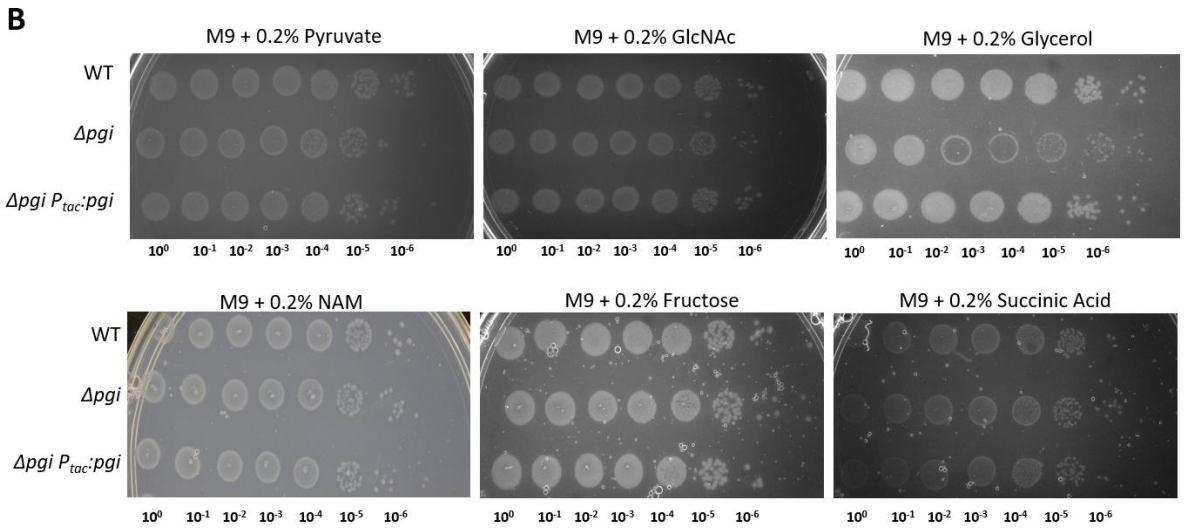

777

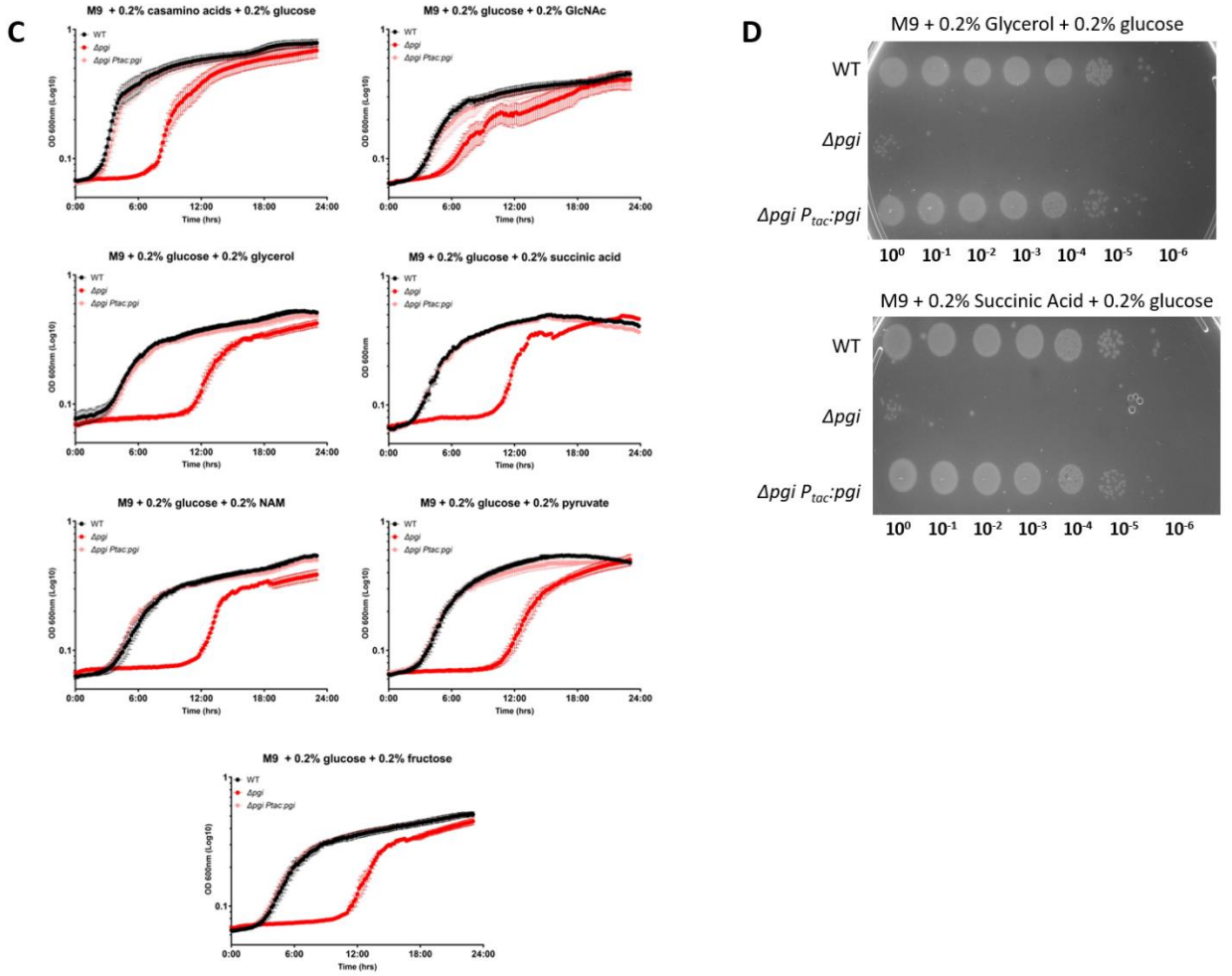

Figure S2: Ability of Δ*pgi* to grow on various carbon sources. A) Growth curves with M9 minimal media and the indicated sole carbon sources. SEM plotted. B) Serial dilutions of overnight cultures grown in M9 + 0.2%CAA plated on M9 agar supplemented with the indicated carbon sources and grown for 18 hours at 37°C. C) Growth curves with M9 minimal media, designated carbon sources, and 0.2% glucose. SEM plotted. D) Serial dilutions of overnight cultures grown in M9 + 0.2%CAA plated on M9 agar supplemented with the designated carbon sources and 0.2% glucose.

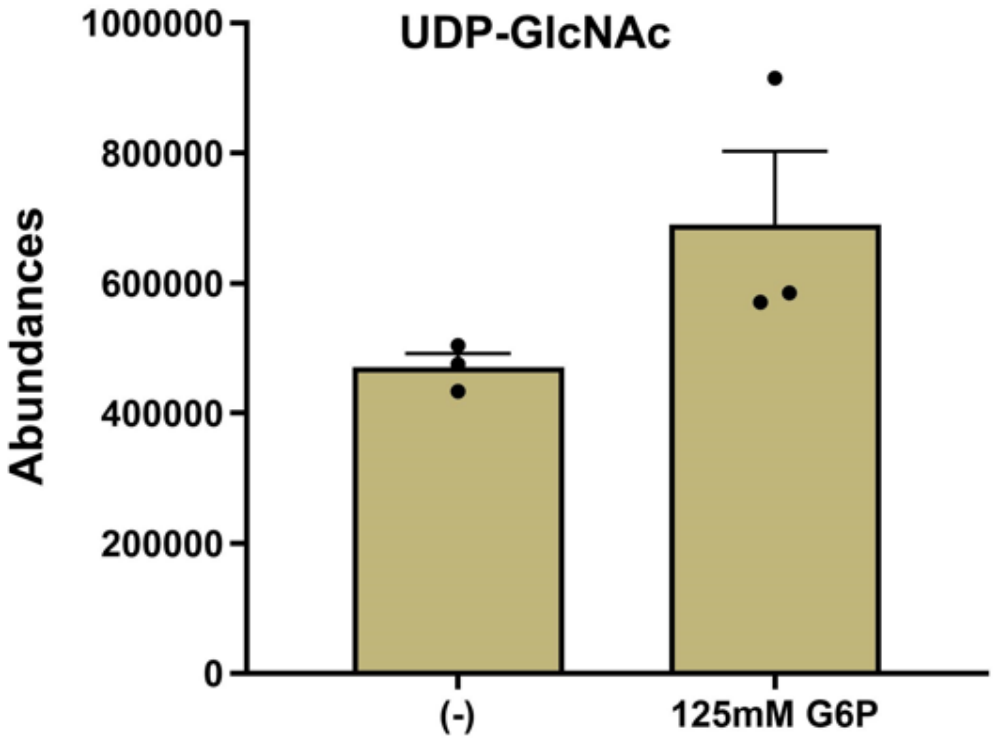

787

788 Figure S3*: In vitro* biochemical abundance of specified metabolites. UDP-GlcNAc levels
789 measured with 125mM G1P addition. SEM plotted with 3 replicates displayed.
790

A

Model	Polar interactions with Glucosamine-1-P	Length of bond (Å) – some residues form multiple bonds with Glucosamine-1-P	Predicted Template Modeling (pTM) score (confidence in structure)	Interface Predicted Template Modeling (ipTM) score (confidence in interface)
0	Arg 330 Lys 348 Tyr 363 Asn 374 Asn 383 – this does not bind N in glucosamine Lys 389	3.0 3.5 2.9, 3.6, 3.7 2.1 3.2, 3.3, 3.4 2.8, 3.0, 3.2, 3.3	0.9556	0.9387
1	Arg 330 Lys 348 Asn 359 Tyr 363 Asn 383 Lys 389	2.9 2.9 3.2 2.5 2.9 2.4, 3.5	0.9558	0.9389
2	Arg 330 Tyr 363 Asn 374 Asn 383 Lys 389	2.9 2.4, 3.3, 3.4 2.0 3.2, 3.5 2.8	0.9553	0.9385
3	Arg 330 Lys 348 Tyr 363 Asn 374 Asn 383 – this binds N in glucosamine Lys 389	3.0 3.5 2.7, 2.9, 3.6 2.1 3.2, 3.3, 3.4 2.8, 3.0, 3.2, 3.3	0.9556	0.9388
4	Arg 330 Lys 348 Tyr 363 Asn 374 Asn 383 Lys 389	2.9, 3.4 2.8 2.5 1.9 3.5 2.8, 3.5	0.9554	0.9384

791

B

Model	Polar interactions with Glucose-1-P	Length of bond (Å) – some residues form multiple bonds with Glucose-1-P	Predicted Template Modeling (pTM) score (confidence in structure)	Interface Predicted Template Modeling (ipTM) score (confidence in interface)
0	Lys 12* Gly 13* Asp 102 Asn 224	2.9 3.1, 3.4 3.5 3.2	0.9553	0.9382
1	Leu 8* Ala 10* Lys 12* Lys 22	3.3 3.5 3.5 2.7, 3.6	0.9555	0.9385
2	Arg 330 His 360 Tyr 363 Asn 374 Asn 383 Lys 389	2.4, 3.4 3.4 2.0 2.8, 3.2 3.3, 3.3 2.7, 3.4	0.9548	0.9375
3	Lys 12* Gly 13* Lys 22 Gln 76 Asp 102 Asn 224	2.6 3.0, 3.4 2.6, 3.5 3.3 2.9 3.0	0.9552	0.9382
4	Arg 330 Lys 348 Asg 359 Tyr 363 Asn 374 Asn 383 Tyr 384* Lys 389	3.3 3.5 3.0 2.6, 3.1 3.0, 3.3 2.9, 3.3, 3.4 3.1 3.1, 3.5	0.9549	0.9376

792

C

Model	Polar interactions with G6P	Length of bond (Å) – some residues form multiple bonds with G6P	Predicted Template Modeling (pTM) score (confidence in structure)	Interface Predicted Template Modeling (ipTM) score (confidence in interface)
0	Asn 374 Ala 377 * Asn 383 His 360 Asn 359 Arg 330 Lys 348 Tyr 363	3.1, 2.8 3.3 2.6, 2.9, 3.0 3.5, 3.4 3.5 2.3, 3.4 3.0 2.5	0.9332	0.9083
1	Ala 377 * Asn 374 Ser 402 Asn 383 His 360 Tyr 363 Arg 330 Lys 348 Lys 389	3.3 2.9, 2.9 3.5 2.3, 3.0, 3.1 3.4 3.6, 2.7 3.4, 2.8 3.1 3.3	0.9342	0.9099
2	Asn 374 Asn 359 His 360 Arg 330 Tyr 363 Lys 348 Lys 389 Ser 402	2.2, 3.2, 3.6 2.8 3.5 2.6 1.9 3.5, 3.5 3.0 3.2	0.9335	0.9080
3	Asn 383 Tyr 363 Arg 330 Asn 374 Val 375 *	3.1 3.1, 3.4 2.3 2.4, 3.0 3.1	0.9336	0.9095
4	Asn 383 Tyr 363 Arg 330 Lys 389 Asn 359 Asn 374 Ala 377 *	2.9, 3.2 2.3 2.3, 3.5 3.3 3.0 2.8, 2.9 3.4	0.9336	0.9095

*interaction with backbone, not side chain

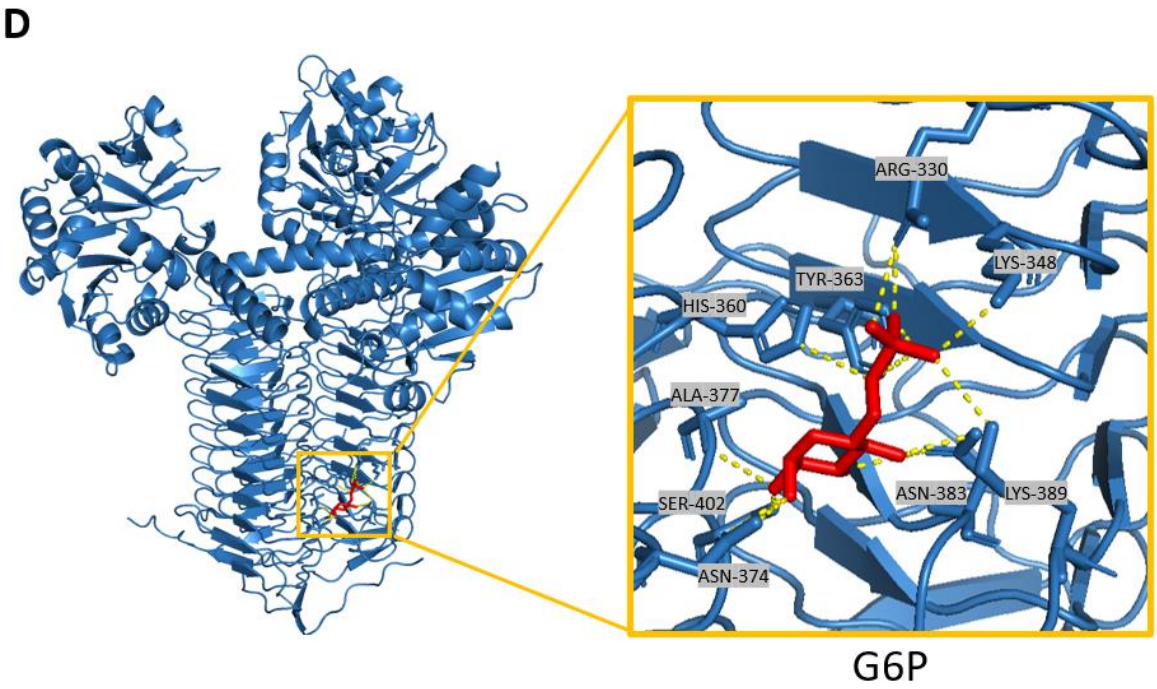

Figure S4: Predicted molecular models of GlmU. A) Predicted models of VCH GlmU with glucosamine-1P with interacting residues denoted, length of bonds, pTM and ipTM scores. Model #3 was the model used above. B) Predicted models of VCH GlmU with glucose-1P with interacting residues denoted, length of bonds, pTM and ipTM scores. Model #4 was the model used above. Highlighted in green are the same interacting residues as the substrate GlcN-1P. C) Predicted models of VCH GlmU with glucose-6P with interacting residues denoted, length of bonds, pTM and ipTM scores. Model #1 was the model used above. Highlighted in green are the same interacting residues as the substrate GlcN-1P. D) Molecular modeling of GlmU binding glucose-6P (red) and the associated polar interactions.

A

```
CLUSTAL O(1.2.4) multiple sequence alignment

sp|P9WMN3|GLMU_MYCTU      MTFPGDTAVLVLAAGPGTRMRSDTPKVLHTLAGRSMLSHVLHAIAKLAPQRLIVVLGHDH  60
sp|P0ACC7|GLMU_ECOLI      -MLNNAMSVVILAAGKGTRMYSDLPKVLHTLAGKAMVQHVIDAANELGAAHVHLVYGHGG  59
sp|Q9KNH7|GLMU_VIBCH      ----MKFSTVILAAGKGTRMHSNMPKVLHTLAGKPMVKHVIDTCNNLGAQNIHLVYGHGG  56
                                 :.::**** **** *: *********: *:.**:.:  :*.  .: :* **.

sp|P9WMN3|GLMU_MYCTU      QRIAPLVGELADTLGRTIDVALQDRPLGTGHAVLCGLSALPDDYAGNVVVTSGDTPLLDA  120
sp|P0ACC7|GLMU_ECOLI      DLLKQALK------DDNLNWVLQAEQLGTGHAMQQAAPFFADD--EDILMLYGDVPLISV  111
sp|Q9KNH7|GLMU_VIBCH      DQMQQALA------NENVNWVLQAQQLGTGHAVDQASPHFQDD--EKILVLYGDVPLISE  108
                          : :   :       . .:: .** . ******:  .   : **   .:::  **.**:.

sp|P9WMN3|GLMU_MYCTU      DTLADLIATHRAVSAAVTVLTTTLDDPFGYGRILRTQDHEVMAIVEQTDATPSQREIREV  180
sp|P0ACC7|GLMU_ECOLI      ETLQRLRDAKP--QGGIGLLTVKLDDPTGYGRITREN-GKVTGIVEHKDATDEQRQIQEI  168
sp|Q9KNH7|GLMU_VIBCH      DTIESLLEAQP--TDGIALLTVVLEDPTGYGRIVRKR-GPVVAIVEQKDASEEQKLIKEV  165
                          :*:  *  ::     .: :**. *:** ***** * .   * .***:.**: .*: *:*:

sp|P9WMN3|GLMU_MYCTU      NAGVYAFDIAALRSALSRLSSNNAQQELYLTDVIAILRSDGQTVHASHVDDSALVAGVNN  240
sp|P0ACC7|GLMU_ECOLI      NTGILIANGADMKRWLAKLTNNNAQGEYYITDIIALAYQEGREIVAVHPQRLSEVEGVNN  228
sp|Q9KNH7|GLMU_VIBCH      NTGVLVATGRDLKRWLAGLNNNNAQGEYYLTDVIAAAHDEGRAVEAVHPSHSIEVEGVND  225
                          *:*:       ::  *: *..**** * *:**:**   .:*: : * * .    * ***:

sp|P9WMN3|GLMU_MYCTU      RVQLAELASELNRRVVAAHQLAGVTVVDPATTWIDVDVTIGRDTVIHPGTQLLGRTQIGG  300
sp|P0ACC7|GLMU_ECOLI      RLQLSRLERVYQSEQAEKLLLAGVMLRDPARFDLRGTLTHGRDVEIDTNVIIEGNVTLGH  288
sp|Q9KNH7|GLMU_VIBCH      RIQLARLERAFQARQAKKLLEQGVMLRDPARFDLRGTLQCGSDVEIDVNVIIEGNVSIGN  285
                          *:**:.*    : . .      ** : ***   :   :  * *. *. .. : *.. :*

sp|P9WMN3|GLMU_MYCTU      RCVVGPDTTLTDVAVGDGASVVR-THGSSSSIGDGAAVGPFTYLRPGTALGADGKLGAFV  359
sp|P0ACC7|GLMU_ECOLI      RVKIGTGCVIKNSVIGDDCEISPYTVVEDANLAAACTIGPFARLRPGAELLEGAHVGNFV  348
sp|Q9KNH7|GLMU_VIBCH      NVVIGAGSILKDCEIDDNTVIRPYSVIEGATVGENCTVGPFTRLRPGAELRDDAHVGNFV  345
                          .  :* .  :.:  :.*.  :   :  ..:.:.  .::***: ****: *  ..::* **

sp|P9WMN3|GLMU_MYCTU      EVKNSTIGTGTKVPHLTYVGDADIGEYSNIGASSVFVNYDGTSKRRTTVGSHVRTGSDTM  419
sp|P0ACC7|GLMU_ECOLI      EMKKARLGKGSKAGHLTYLGDAEIGDNVNIGAGTITCNYDGANKFKTIIGDDVFVGSDTQ  408
sp|Q9KNH7|GLMU_VIBCH      EMKNARLGEGSKANHLTYLGDAEIGKGVNVGAGVITCNYDGANKHKTVIGDDVFVGSDCQ  405
                          *:*:: :* *:*. ****:***:**.  *:**. :  ****:.* :* :*..* .***

sp|P9WMN3|GLMU_MYCTU      FVAPVTIGDGAYTGAGTVVREDVPPGALAVSAGPQRNIENWVQRKRPGSPAAQASKRASE  479
sp|P0ACC7|GLMU_ECOLI      LVAPVTVGKGATIAAGTTVTRNVGENALAISRVPQTQKEGWRRPVKKK------------  456
sp|Q9KNH7|GLMU_VIBCH      LVAPVTIGNGATIGAGTTLTKNVAEGELVITRAPERKIAGWQRPAKKK------------  453
                          :*****:*.**  .***.: .:*  . *.::  *: :  .* :  :

sp|P9WMN3|GLMU_MYCTU      MACQQPTQPPDADQTP      495
sp|P0ACC7|GLMU_ECOLI      ----------------      456
sp|Q9KNH7|GLMU_VIBCH      ----------------      453
```

B

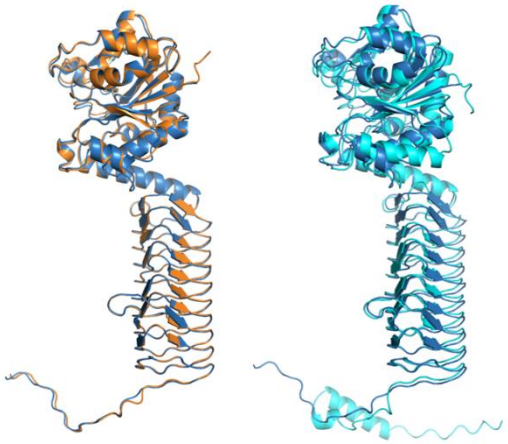

RMSD = 0.31 Å

RMSD = 1.22 Å

C

	M. TB	E. coli	VCH
M. TB	100	38.68	40.04
E. coli	38.68	100	67.55
VCH	40.04	67.55	100

Figure S5: Structural alignments of GlmU. A) Multiple amino-acid sequence alignments of *M.Tb, E.coli,* and *V. cholerae* with conserved residues denoted, using Clustal. B) GlmU monomer structural alignment. $GlmU^{VC}$ is blue, $GlmU^{EC}$ is depicted in orange, and $GlmU^{Mtb}$ is in teal. RMSD, root mean squared deviation, is a measure of how closely two alignments match; RMSD < 2.5 is a reasonable alignment. C) Percent Identity Matrix, created by Clustal2.1 shows alignment similarity across species.

Strain	Description	Source or Reference
WT*	Wild-type *V. cholerae* N16961 El Tor	Heidelberg JF, *et. al.*, 2000
MK1*	Δ*pgi* (vc0374)	Keller MK, *et. al.*, 2023
MK4	Δ*pgi* P_{tac}- *pgi*	Keller MK, *et. al.*, 2023
MK12	Δ*pgi* P_{tac}- *nagB* (vca1025)	This study
MK13*	Δ*pgi* Δ*pgcA* (vc2095)	This study
MK14	Δ*pgi* P_{tac}- *pgcA*	This study
MK15	Δ*pgi* P_{tac}- *glmS* (vc0487)	This study
MK16	Δ*pgi* pHL: *glmU* (vc2762)	This study
MK110	*E. coli* SM10 λpir conjugation strain	Ferrières L, *et. al.*, 2010
MK120	*E. coli* MFD pir conjugation strain	Ferrières L, *et. al.*, 2010
MK130	E. coli BL21 protein purification strain	Novagen

* = checked via whole genome sequencing

Table S1: Strain list used in this study. * = checked via whole genome sequencing

Plasmid	Description	Source or reference
pTD101	chromosomal lacZ insertion with IPTG induction	Obando MA, *et. al.*, 2024
pTOX5	gene deletion construct	Lazarus JE, *et. al.*, 2019
pET28a	6xHIS-SUMO tagged protein purification vector	Obando MA, *et. al.*, 2024
pHL100mob	Non-integrative, high copy number plasmid with IPTG induction.	Mett H, *et. al.*, 1980
pTD101 P_{tac} - *nagB*	*nagB* overexpression with whole gene amplification using primers 7 and 8	This study
pTD101 P_{tac} - *pgcA*	*pgcA* overexpression with whole gene amplification using primers 9 and 10	This study
pTD101 P_{tac} - *glmS*	*glmS* overexpression with whole gene amplification using primers 11 and 12	This study
pHL100mob*: glmU*	*glmU* overexpression with whole gene amplification using primers 13 and 14	This study
pET28a glmU	GlmU protein purification strain	This study
pTOX pgcA	*pgcA* deletion by amplifying 500bp up and down stream of the gene using primers 15-18	This study

Primer description	Sequence (5'-3')	Number
pTD101fwd	ggcaaatattctgaaatgagctgt	1
pTD1010rev	cCAGATCTTAATTAAGGtgcgttct	2
pTOXfwd	tcgctcgcaaacctg	3
pTOXrev	gatcgagctcgagacg	4
pHL100fwd	cggataacaatttcacacagga	5
pHL100rev	gctgaaaatcttctctcatccgc	6
nagB pTD101fwd	aacagaccatggaattcgagctcggtacccAGGAGGctgactgaATGAGACTTATCC	7
nagB pTD101rev	atgcctgcaggtcgactctagaggatccccTTAGAAGCCTAC	8
pgcA pTD101fwd	aacagaccatggaattcgagctcggtacccAGGAGGctgactgaATGGCTATGCACCCT	9
pgcA pTD101rev	CGTG	10
glmS pTD101fwd	atgcctgcaggtcgactctagaggatccccTTATAAACCCGCGTCTTTAAACACTTGGT	11
glmS pTD101rev	TTACG	12
glmU pHL100fwd	aacagaccatggaattcgagctcggtacccAGGAGGctgactgaATGTGTGGAATTGTT	13
glmU pHL100rev	GGTGC	14
pgcA up500fwd	atgcctgcaggtcgactctagaggatccccTTACTCGACAGTTACCGCTTTAG	15
pgcA up500rv	aacagaccatggaattcgagctcggtacccAGGAGGctgactgaATGAAATTCAGTACG	16
pgcA dwn500fwd	GTAATTCTCG	17
pgcA dwn500rev	atgcctgcaggtcgactctagaggatccccTTATTTCTTTTTCGCCGGACGCTGC	18
pgcA flankfwd	ggcggggttttttcgttgatcacgtacgatCGAAAGGGATAGTCGTAAGCAAAGATGC	19
pgcA flankrev	TCATCATTATTACTCGAGTGCGGCCGCATTAAGTGACATCCTTTCTTTAAATTT	20
pgcA internalfwd	CACATAAAATAAAACC	21
pgcA internalrev	TAATGCGGCCGCACTCGAGTAATAATGATGATGTGATGAAATGAATCAGG	22
MK chromolacZfw	CTTGCCTGCCGAGTTTGAGT	23
MK chromolacZrev	CTGCCACTGGTAATGCGAGC	24

Table S2: Oligos used in this study.